CHEMISTRY OF MATERIALS

pubs.acs.org/cm Article

A Cobalt–Platinum–Ruthenium System for Acidic Methanol Oxidation

Hongbin Xu,[#] Daniel J. Zheng,[#] Haldrian Iriawan, Jen-Hung Fang, Junghwa Kim, Xiao Wang, Yuriy Román-Leshkov,* Ju Li,* and Yang Shao-Horn

Cite This: Chem. Mater. 2024, 36, 6938–6949 Read Online

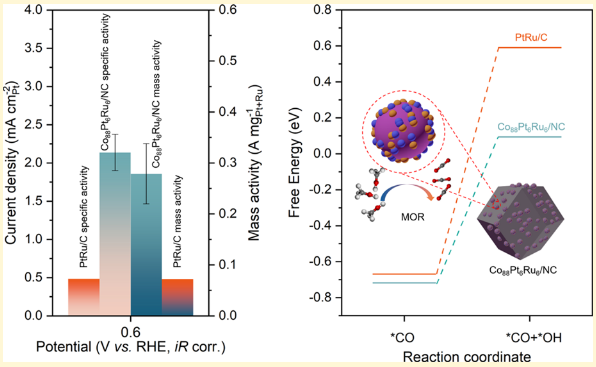

ABSTRACT: The electrochemical oxidation of methanol is a crucial catalytic reaction in direct methanol fuel cells (DMFCs). Platinum (Pt) or Pt-alloy electrocatalysts have dominated the space, especially in acidic conditions, and different design strategies are needed to achieve both high specific and mass activities. Herein, we comprehensively developed a system of cobalt–platinum–ruthenium nanoparticles within three-dimensional nitrogen-doped porous carbon (Co–Pt–Ru/NC) as an efficient methanol oxidation reaction (MOR) catalyst and investigated different factors such as Pt loading and acid treatment. We found that the intermediate Pt loading displayed MOR activity as low as 0.3 V_{RHE} (versus the reversible hydrogen electrode) and exhibited the highest specific activity (2.1 ± 0.2 mA cm_{Pt}^{-2}) and mass activity (0.28 ± 0.06 A mg_{Pt+Ru}^{-1}) at 0.6 V_{RHE}, which is 4.4 times and 3.9 times higher than the commercial PtRu/C catalysts, respectively. Furthermore, the catalytic activity remains nearly unchanged in acid-treated catalysts after cobalt is partially dissolved in acidic conditions. Through density functional theory calculations of the MOR on our catalyst surface, the enhanced activity was found to originate from cobalt weakening CO adsorption on Pt sites, while simultaneously facilitating OH formation on Ru sites, effectively lowering the energy barrier for the rate-determining step in the MOR and showing promising potential for DMFCs.

■ INTRODUCTION

Methanol (CH_3OH) is a valuable chemical both in industrial synthesis and as a fuel. In recent years, significant work has been dedicated to improving the efficiency of methanol production by CO_2 reduction and achieving the goal of net-zero emission.[1−4] As more methanol becomes available, a natural question arises, owing to its high energy density and liquid state, the design of efficient direct methanol fuel cells (DMFCs), in which methanol is a medium for storing and converting electrical energy from chemical energy.[5,6] The volumetric energy density of methanol is around 15.6 MJ L^{-1}, which is three times higher compared to that of liquid H_2 (4.7 MJ L^{-1}),[7] making these devices particularly suited for portable applications where size can be a major limitation. Nevertheless, the development of DMFCs has been slow since the early studies of this device in the 1950s,[8] primarily due to the 6 e^- required for the methanol oxidation reaction (MOR, theoretical potential of 0.02 V), $CH_3OH + H_2O \rightleftharpoons CO_2 + 6(H^+ + e^-)$, leading to sluggish kinetics at the anode.[9,10]

Tremendous efforts have been dedicated to designing active electrocatalysts for the methanol oxidation reaction (MOR). Platinum (Pt) and Pt-based catalysts have dominated electrocatalyst design for this reaction,[11−13] especially within DMFC devices,[14−16] due to their high acid resistance and relatively lower overpotential compared to other transition metal catalysts.[17,18] However, in contrast to the nearly negligible overpotential of the hydrogen oxidation reaction that occurs at the anode in a hydrogen fuel cell,[19−22] the overpotential for MOR on Pt surfaces (>0.45 V with state-of-the-art catalysts[23−25]) still greatly limits the efficiency of DMFCs. As such, considerable efforts have been made toward engineering Pt surfaces and nanoparticles to increase the MOR activity. For example, Lee et al. have reported the significant role of surface steps on Pt nanoparticles for catalyzing the MOR, resulting in ~200% enhanced activity with increasing surface steps on ~2 nm Pt nanoparticles.[26] Also, Suntivich et al. have shown that the catalytic activity of $Au_{0.5}Pt_{0.5}/C$ nanoparticles could be tuned by controlling the surface Pt to Au ratio, where a ~30 to 70 Pt to Au ratio showed 2 orders of magnitude higher MOR activity compared to pure Pt/C.[27] Moreover, the high cost and the scarcity of Pt still hinder the practical application of

Received: April 4, 2024
Revised: June 20, 2024
Accepted: June 27, 2024
Published: July 3, 2024

https://doi.org/10.1021/acs.chemmater.4c01008
Chem. Mater. 2024, 36, 6938–6949

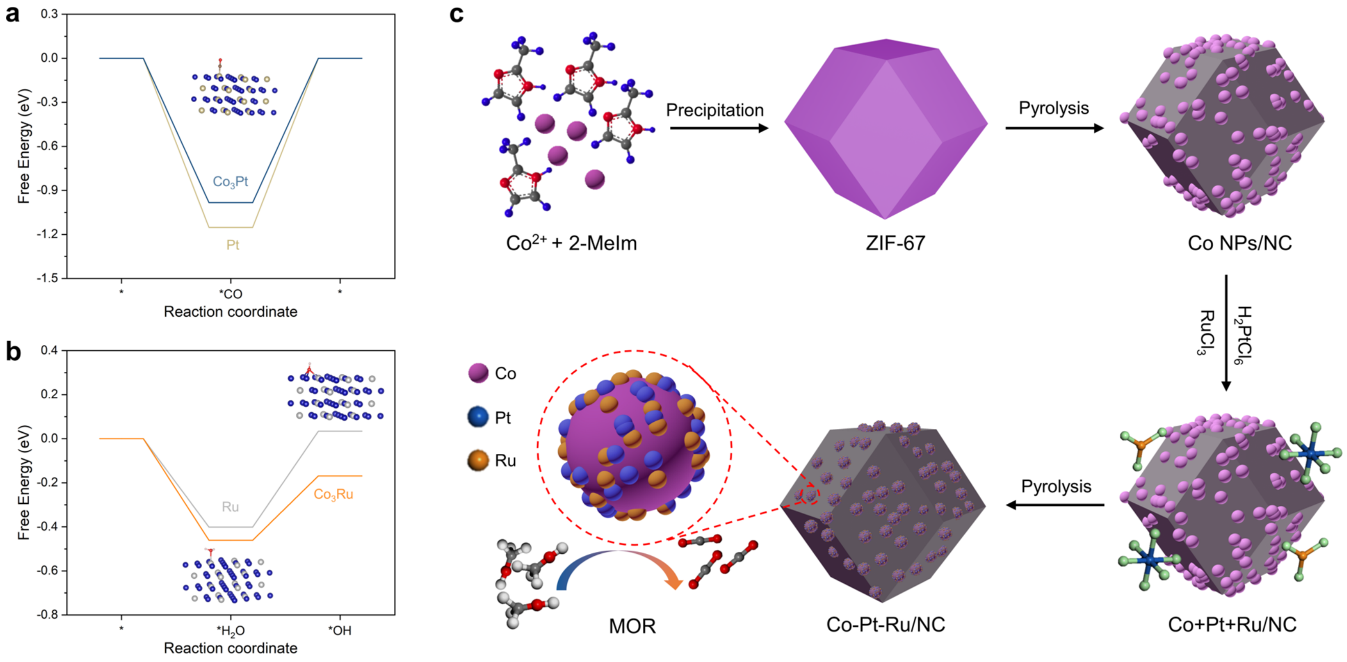

Figure 1. Free energy diagrams of (a) Pt and Co_3Pt for CO adsorption, and (b) Ru and Co_3Ru for H_2O and OH adsorptions. The free energy values are referenced to 1 bar H_2 and $H_2O_{(l)}$. (c) Schematic of the Co−Pt−Ru/NC synthesis.

DMFCs. Therefore, a deeper understanding of MOR electrocatalysts is required for the rational design of low Pt loading or Pt-free electrocatalysts for DMFC use.

PtRu is the current benchmark electrocatalyst for the MOR.[28,29] Previous studies on the surfaces of well-defined Pt_xRu_{1-x} alloys have shown that the addition of Ru to Pt enhances the MOR activity by ∼30 times by decreasing the coverage of poisoning CO species, leading to an optimal in MOR activity when there is a specific balance between the Pt and Ru ratios that optimizes the rate of methanol dehydrogenation on Pt sites and rate of formation of surface oxygenated species on Ru sites, strongly supporting the bifunctional effects of Pt and Ru for promoting the MOR.[29] Density functional theory (DFT) calculations have further supported the proposed bifunctional effect, as the presence of Ru in PtRu has been calculated to facilitate water dissociation to form surface-bound OH (*OH), further accelerating the oxidation of coadsorbed *CO in the final reaction step $*CO + *OH \rightleftharpoons CO_2 + H^+ + e^-$.[30,31] Leveraging the bifunctional effect, other alloys have also been developed for the MOR, such as PtSn,[32−34] which shows nearly comparable activity to PtRu. However, a significant amount of MOR catalyst development has centered on different synthesis strategies to increase the activity of PtRu for the MOR. For example, Chen et al. have synthesized Ru_1Pt_n alloys with Ru atomically dispersed in Pt nanocrystals.[35] However, the activity of Ru_1Pt_n is similar to that of Pt/C catalyst at 0.5 V_{RHE}, as Pt is the main component in Ru_1Pt_n. Conversely, Poerwoprajitno et al. created single Pt-atom-on-Ru catalysts by spreading Pt islands on Ru branches.[36] Although this catalyst shows a lower onset potential than that of Ru_1Pt_n, the mass activity is comparable to that of commercial PtRu/C when normalized by the noble metal mass. In either case, there is always an abundance of underutilized Pt or Ru sites. Thus, the atomic dispersal strategy, where an electroactive component of the alloy is used as the host may be extreme as it can lead to the underutilization of Pt or Ru. To achieve both high specific activity and mass activity for the MOR, suitable support for both Pt and Ru, as well as proper loading of Pt and Ru, should be explored in order to maximize the utilization of both metals. As such, ternary metal composites are a reasonable system, as Pt and Ru loadings can be effectively varied. There are several reports on ternary metal composites for the MOR; however, the onset potential for the MOR of these catalysts is still higher than 0.6 V_{RHE} due to the absence of Ru or the heterogeneous distribution of Ru.[37,38] Moreover, when transition metals are employed in acids, one unavoidable problem is that the catalyst will gradually transform under acidic conditions through processes such as rearrangement and partial dissolution.[39−42] Thus, finding a suitable substrate, regulating the loading of Pt, and investigating the change of catalyst under acidic conditions are of significance for the rational design of MOR catalysts.

D-band theory has been demonstrated to provide guidance for the experimental results and the explanation of surface−adsorbate interaction strengths.[43] Previous DFT calculations have shown that the surface Pt d-band shifts to lower energy compared to that of pure Pt(111) when cobalt (Co) serves as a subsurface,[44] which indicates that the strong adsorption of *CO on Pt sites could be alleviated to enhance the CO resilience of catalysts.[45] On the other hand, ΔE_O can be regulated by a downshift of about 0.51 eV by replacing Ru with Co on a Ru surface on the top of a Co substrate.[46] Therefore, based on scaling relations,[47] *OH adsorption might also be stronger on Ru sites with Co substitution, which could further facilitate CO removal on the catalyst surface. As such, Co appears to be a promising candidate to serve as a host substrate for Pt and Ru to increase the MOR activity. Herein, we synthesize a ternary system composed of cobalt−platinum−ruthenium nanoparticles within three-dimensional nitrogen-doped porous carbon (Co−Pt−Ru/NC) for the MOR. The system allows for easy adjustment of the Pt loading, with optimal performance observed at intermediate loading levels. Benefiting from the optimized binding energy of the intermediates, $Co_{88}Pt_6Ru_6$/NC demonstrates MOR activity

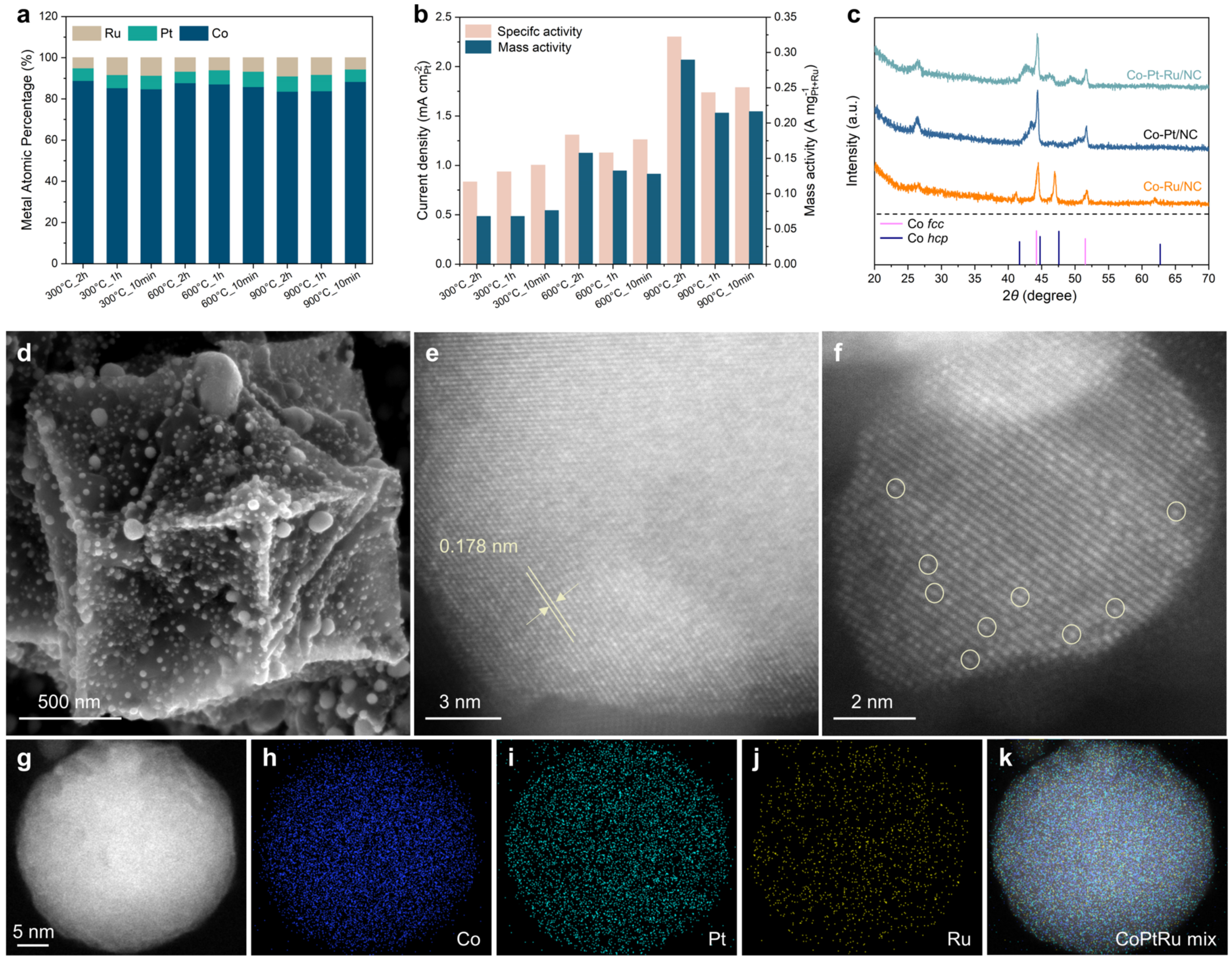

Figure 2. Optimization of synthesis and structural characterization of Co−Pt−Ru/NC. (a) Metal atomic percentages measured using ICP-OES of Co, Pt, and Ru in Co−Pt−Ru/NC synthesized under different conditions. (b) Specific and mass activities at 0.6 V vs RHE of Co−Pt−Ru/NC synthesized under different conditions. (c) XRD patterns of Co−Ru/NC, Co−Pt/NC, and Co−Pt−Ru/NC catalysts. SEM image (d), HAADF-STEM images (e and f, circled atoms are Pt and Ru), and corresponding EDX mapping (g−k) of Co−Pt−Ru/NC. The normalized atomic metal compositions were Co: 71.2%, Pt: 14.1%, and Ru: 14.7%.

as low as 0.3 V_{RHE}, while commercial PtRu/C displays no activity at this voltage. The most active catalyst achieves 2.1 ± 0.2 mA cm_{Pt}^{-2} and 0.28 ± 0.06 A mg_{Pt+Ru}^{-1} at 0.6 V_{RHE}, which are 4.4 and 3.9 times higher than the respective metrics of PtRu/C. Acid treatment results reveal that the material maintains superior activity compared to PtRu/C, even after soaking in 0.1 M $HClO_4$ for 200 h. Moreover, DMFCs constructed with optimized $Co_{88}Pt_6Ru_6$/NC as the anode catalyst also deliver a higher peak power density than when PtRu/C is used, even when the anode catalyst loading is decreased to 30% of the loading of the commercial benchmark.

■ RESULTS AND DISCUSSION

Design and Characterization of Co−Pt−Ru/NC. To choose a suitable support for Pt and Ru, DFT calculations were performed to evaluate the binding energy of the key intermediates *CO and *OH. Calculations of ternary and higher mixtures of metals are not convenient due to their complexity and computational cost. For a simple and quick insight, we compared the binding energies of *CO on Pt and Co_3Pt (Figure S1). As shown in Figure 1a, *CO shows weaker adsorption on the Co_3Pt surface (−0.98 eV) than on Pt (−1.15 eV). Furthermore, the OH formation processes on Ru and Co_3Ru were also evaluated (Figure S2). First, H_2O is more easily adsorbed on the Ru sites of Co_3Ru, as indicated by the more negative binding energies. The energy barrier for the formation of *OH is lower on the Co_3Ru (0.29 eV) surface than on pure Ru (0.43 eV) (Figure 1b). These results imply that Co not only weakens the adsorption of CO on Pt sites but also strengthens the formation of OH on Ru sites, which makes Co an ideal support for Pt and Ru. Co−Pt−Ru/NC catalysts were synthesized via a two-step pyrolysis method, as illustrated in Figure 1c. First, after obtaining ZIF-67 (Figure S3), Co nanoparticles within nitrogen-doped carbon (Co NPs/NC, Figure S4) were prepared by pyrolysis of ZIF-67 at 1000 °C under Ar atmosphere for 2 h followed by cooling naturally, which allowed the adsorption of Pt^{4+} (from $H_2PtCl_6{\cdot}xH_2O$) and Ru^{3+} (from $RuCl_3{\cdot}xH_2O$) ions. The Pt^{4+} and Ru^{3+} adsorbed Co nanoparticle precursors (Co + Pt + Ru/NC, Figure S5) were then annealed at 900 °C for 2 h under an Ar atmosphere and cooled naturally to form the final product Co−Pt−Ru/NC.

https://doi.org/10.1021/acs.chemmater.4c01008
Chem. Mater. 2024, 36, 6938−6949

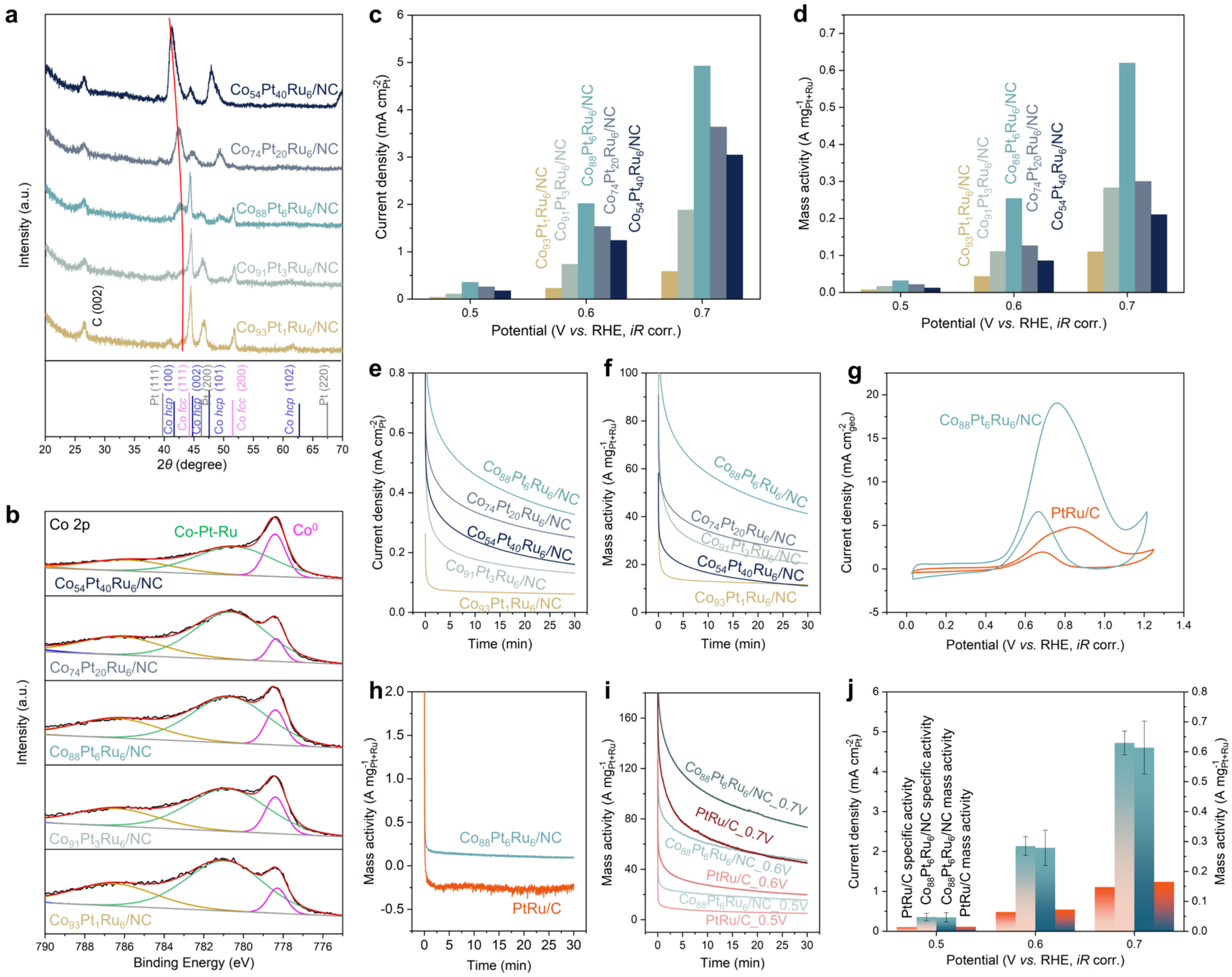

Figure 3. MOR performance and characterization of different Pt-loaded catalysts. (a) XRD patterns of different Pt-loaded catalysts. (b) XPS spectra of Co 2p for different Pt-loaded catalysts catalysts. (c−f) Electrocatalytic performances of different Pt-loaded catalysts. The specific activity (c) and mass activity (d) of the CV at potentials of 0.5, 0.6, and 0.7 V_{RHE}. The specific activity (e) and mass activity (f) of the CA at 0.6 V_{RHE}. (g−j) MOR performance of the optimized $Co_{88}Pt_6Ru_6/NC$ compared with that of a commercial PtRu/C catalyst. CV curves were recorded at 0.1 M $HClO_4$ with 1 M CH_3OH (g). CA results at 0.3 V vs RHE (h), the mass activity (i) of CA at 0.5−0.7 V_{RHE}. Specific activity and mass activity of the CV at potentials of 0.5, 0.6, and 0.7 V_{RHE} (j).

The synthesis conditions were first explored by changing the heating temperature and time during the second pyrolysis (300, 600, and 900 °C; 10 min, 1, and 2 h). The X-ray diffraction (XRD) patterns showed that the two peaks near 44° become closer and more obvious as the heating temperature increases because high temperatures can improve the Co−Pt−Ru mix better (Figure S6). The morphology of the prepared products was examined using scanning electron microscopy (SEM, Figure S7). The samples treated below 300 °C showed rough surfaces and large chucks because of incomplete carbonization and poor mixing, while the samples treated at higher temperatures and longer pyrolysis times led to uniform nanoparticles. The atomic percentages of Co, Pt, and Ru in the materials under different synthesis conditions were examined using inductively coupled plasma optical emission spectrometry (ICP−OES). There were no significant differences in the metal loadings resulting from the different synthesis conditions (Figures 2a and S8), indicating that the difference in performance was not due to different loadings. The residual Cl in the samples was examined by ion chromatography (Figure S9), which showed that almost no Cl was present in catalysts synthesized at different temperatures, excluding the effect of Cl on activity. Cyclic voltammetry (CV) polarization curves (Figure S10) of the materials showed that the catalyst synthesized at 900 °C for 2 h had the highest specific and mass activities. Figure 2b compares the specific and mass activities of all samples at 0.6 V_{RHE}, which shows a monotonic increase in the MOR activity with heating temperatures. For the samples heated at lower temperatures (e.g., 300 °C), two superimposed peaks in the forward CV scan (i.e., anodic direction) were observed, most likely indicating poor mixing of the metals, consistent with the XRD results. Chronoamperometry (CA) results also showed poor activity of the materials prepared at 300 °C. The material heat-treated at 600 °C for 2 h exhibited activity similar to that of the materials treated at 900 °C at 0.6 V_{RHE}, but a lower activity at 0.7 V_{RHE} (Figure S11). As the most active synthesis conditions were found to occur when the Co + Pt + Ru/NC precursor was heated at 900 for 2 h, these synthesis conditions were adopted for future studies. Co−Pt/NC and Co−Ru/NC were prepared to better understand the effects of Pt and Ru doping (Figure 2c). The presence of Pt induces a Co peak shift toward lower 2θ, most likely due to the strain imparted by the larger atomic radius of Pt. As the doping of Ru can lead to a partial phase change of Co from face-centered cubic (*fcc*) to the hexagonal close-packed (*hcp*) polymorph,[48] the new peak near 46.4° upon heating at higher temperatures can be explained by the local transformation *of* *fcc*-Co to *hcp*-Co upon Ru substitution.

The morphology of ZIF-67 was polyhedral, and Co−Pt−Ru/NC maintained this shape after pyrolysis (Figure S12). During the first pyrolysis, the carbonization process made the ZIF-67 hollow, and the second pyrolysis made the Pt and Ru dope into Co nanoparticles. The nanoparticles anchored on the hollow carbon skeleton (Figure S13) are Co−Pt−Ru nanoparticles (denoted as $Co_{88}Pt_6Ru_6$/NC, according to the nominal composition, Figure 2d). The atomic structure of the nanoparticles was further explored by high-angle annular dark-field scanning transmission electron microscopy (HAADF-STEM), where the interplanar spacing of $Co_{88}Pt_6Ru_6$/NC was measured to be 0.178 nm (Figure 2e), which matches well with the (200) planar spacing of *fcc*-Co (0.177 nm). The nanoparticles also appear to be covered by an adventitious carbon layer (Figure S14a), which may have acted to prevent aggregation during the second thermal treatment. To obtain a clear view, bright-field (BF) and dark-field (DF) images cross-validated the presence of Pt and Ru within a Co host as a dispersal of higher-intensity atoms (darker atoms in BF and brighter atoms in DF) within the lower-intensity Co matrix can be observed (Figure S14b−e). A proportion of the atoms within a nanoparticle showed a higher intensity than the rest, which, coupled with the similar (200) interplanar spacing between $Co_{88}Pt_6Ru_6$/NC and *fcc*-Co, strongly suggests that Pt and Ru were successfully incorporated into the Co host (Figures 2f and S14f). Energy-dispersive X-ray spectroscopy (EDX) elemental mapping analysis revealed that Co, Pt, and Ru were homogeneously distributed throughout the structure (Figure 2g−k). EDX mapping also confirmed the existence of carbon and nitrogen as conductive supports (Figure S15). The normalized atomic metal compositions of Pt and Ru are higher than those measured from ICP-OES results (Figures S16 and S17), which might be attributed to nonuniform alloying in some nanoparticles measured using EDX, as ICP-OES takes a representative average across the entire synthesized powder. We note that while Co atoms can be observed in pure Co NPs/NC (Figure S18), imaging the interplanar spacing of $Co_{88}Pt_6Ru_6$/NC can be potentially challenging due to scattering from the disordered incorporation of Pt and Ru (Figure S19).

Tuning Pt Loading in Co−Pt−Ru/NC. Considering the price of Pt, the goal of Pt-alloy catalyst design is always to minimize Pt usage, while maximizing activity and durability. Therefore, we aimed to optimize the material for catalyzing the MOR by tuning the Pt loading in Co−Pt−Ru/NC by changing the amount of $H_2PtCl_6{\cdot}xH_2O$ during the adsorption step at ambient conditions, while maintaining the same absolute Ru loading, as confirmed by ICP-OES results (Figure S20). The prepared samples were denoted as $Co_{93}Pt_1Ru_6$/NC, $Co_{91}Pt_3Ru_6$/NC, $Co_{88}Pt_6Ru_6$/NC, $Co_{74}Pt_{20}Ru_6$/NC, and $Co_{54}Pt_{40}Ru_6$/NC, according to their nominal metal atomic compositions during synthesis. The XRD patterns (Figure 3a) show that with the addition of a small Pt amount, the $Co_{93}Pt_1Ru_6$/NC has almost the same XRD pattern as Co−Ru/NC, albeit with a small hump (43.1°) at the left of the Co peak, which matches closely with the (111) reflection of Co_3Pt. With higher Pt loading, the intensity of the small hump at 43.1° increased, and another peak related to the Co_3Pt (200) reflection appeared at 49.7°, as can be seen for $Co_{88}Pt_6Ru_6$/NC. Also, all peaks progressively shifted toward the left as Pt loading increased, which suggests that more Pt was doped into the Co owing to the higher interplanar spacing of Pt compared to Co_3Pt (or Co−Ru) for the same planes. However, if excessive Pt precursor was added, the two peaks around 43 and 44° merged into one peak, which also occurred, similar to the other two peaks located at around 50 and 51°. The fact that the two asymmetric peaks at 41.3 and 47.9° for $Co_{54}Pt_{40}Ru_6$/NC could be deconvoluted into two peaks also demonstrates this point. In fact, new peaks at around 41.3, 47.9, and 70° were observed for $Co_{54}Pt_{40}Ru_6$/NC, which correspond closely to a Pt-rich phase (interpreted from their close proximity to the (111), (200), and (220) reflections of pure Pt, respectively), most likely indicating that Pt alloyed with Co. In this case, Pt is the main support instead of Co, and thus, the $Co_{74}Pt_{20}Ru_6$/NC composition demarcates a transition between the host Pt-poor phase at lower Pt loading and the host Pt-rich phase at high Pt loading. X-ray photoelectron spectroscopy (XPS) was conducted to examine the chemical states of the different elements (Figure S21), which also confirmed the presence of Co, Pt, and Ru. The peak fitting of Co 2p from $Co_{88}Pt_6Ru_6$/NC was composed of three peaks centered at 778.4, 780.8, and 786.6 eV (Figure 3b), which can be attributed to Co^0 in the nanoparticle,[49] alloyed Co in Co−Pt−Ru,[50] and a satellite peak, respectively, which are consistent with a previously reported work.[45] The Co peak of Co−Pt−Ru shifted positively with increasing Pt loading (0.50 eV from $Co_{93}Pt_1Ru_6$/NC to $Co_{54}Pt_{40}Ru_6$/NC) potentially due to the stronger interaction between Co and Pt with more Pt in the system. The Pt 4f peak in these samples can be deconvoluted into two pairs of doublets, including Pt^0 and Pt^{2+}. Similarly, the Ru 3p peak could be fitted by Ru^0 and RuO_2 for both Ru $3p_{3/2}$ and Ru $3p_{1/2}$. However, the Pt and Ru peaks did not display a clear trend, most likely due to the complexity of the system.

The CV curves of methanol oxidation of the materials with different Pt loadings were normalized by the Pt electrochemically active surface area estimated through the hydrogen underpotential deposition region (Figure S22) to give the specific activity and by the Pt + Ru mass loading to give the mass activity. Both specific (Figures 3c and S23a) and mass activity (Figures 3d and S23b) showed a volcano trend as a function of Pt loading, giving an optimal composition of $Co_{88}Pt_6Ru_6$/NC, which exhibited the highest MOR activity at 0.5, 0.6, and 0.7 V_{RHE}. CA measurements were also carried out on these materials at different potentials from 0.4 to 0.7 V_{RHE} in 0.1 V increments (Figures 3e,f and S24 and S25), where the trend of Pt-loading-dependent activity is in agreement with the CV results. For example, both the specific and mass current in the CA measurements at 0.6 V_{RHE} first increased with increasing Pt loading, reaching a maximum with $Co_{88}Pt_6Ru_6$/NC before decreasing with further increased Pt loading. The volcano trend in the MOR activity as a function of Pt loading can be explained by considering that a low concentration of Pt will lead to a small proportion of surface Pt atoms adjacent to the surface Ru atoms, limiting the ability to promote CO oxidation compared to pure Pt. When the Pt loading is increased, statistically, there will be more exposed surface Pt

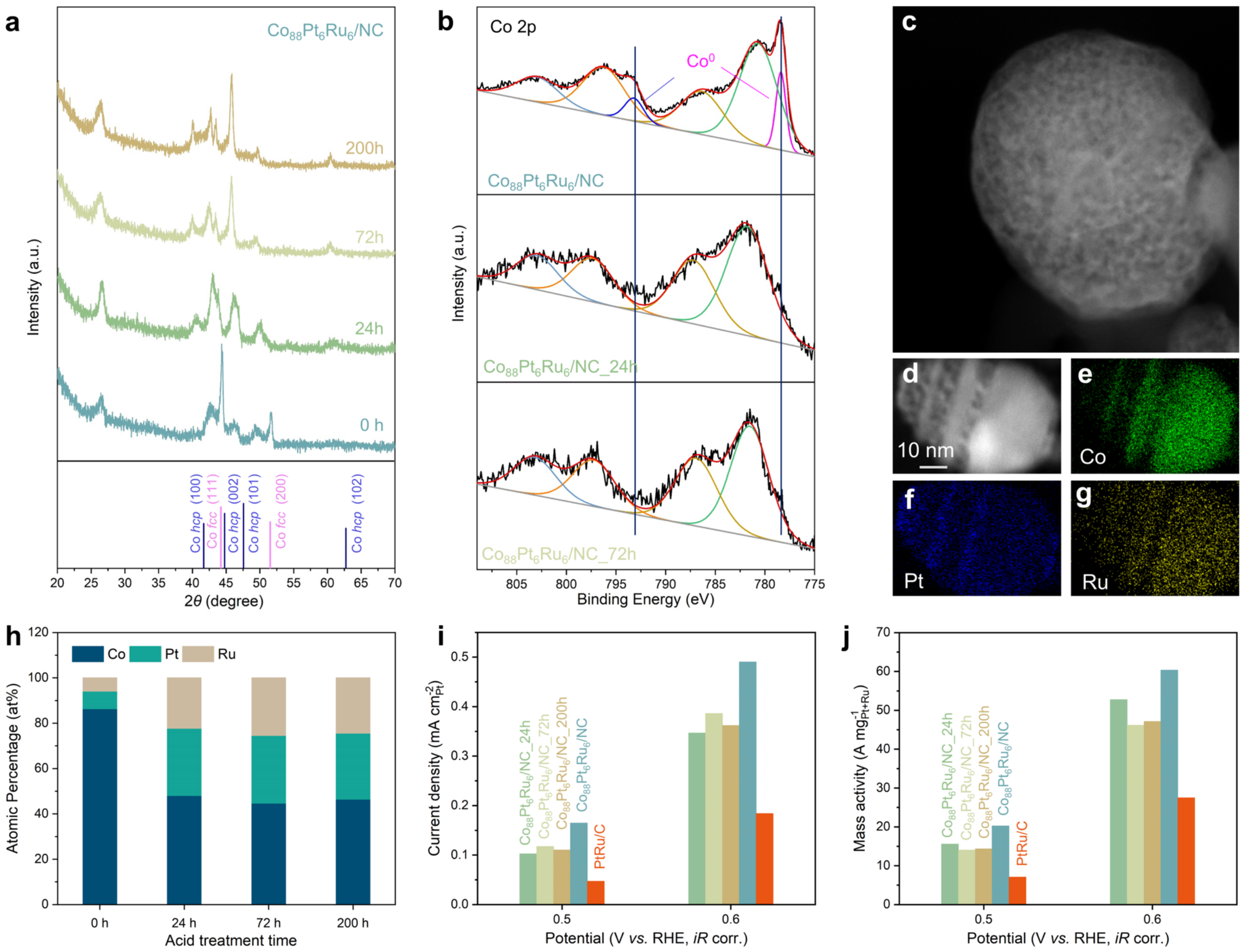

Figure 4. Characterization and electrocatalytic activity of $Co_{88}Pt_6Ru_6/NC$ after acid treatment. (a−h) Characterization of $Co_{88}Pt_6Ru_6/NC$ after acid treatment. XRD patterns (a) and Co 2p XPS spectra (b). HAADF-STEM image of $Co_{88}Pt_6Ru_6/NC\_24h$ (c) and EDX mapping of $Co_{88}Pt_6Ru_6/NC\_24h$ during transition (d−g). Metal atomic percentages obtained from ICP-OES (h). (i−j) CA results at 10 min under 0.5 and 0.6 V_{RHE}. The specific (i) and mass activities (j).

atoms adjacent to Ru atoms, which can synergistically enhance CO oxidation and, therefore, the MOR rate. Upon further increasing Pt, the proportion of Pt atoms adjacent to Ru atoms decreased, losing the synergistic effects of both metals and decreasing activity. Furthermore, one of the obvious problems with excessive Pt is that the mass activity decreases since many Pt atoms in the nanoparticles are underutilized. Also, a fixed Ru loading may cause surplus Pt atoms to aggregate, reducing dispersion and making the nanoparticles more susceptible to CO poisoning, as observed for $Co_{54}Pt_{40}Ru_6/NC$. ICP-OES indicated that the atomic ratio of Pt and Ru in $Co_{88}Pt_6Ru_6/NC$ is close to 1:1, which also explains its excellent activity.

To benchmark the MOR activity of $Co_{88}Pt_6Ru_6/NC$, commercial PtRu/C (Pt/Ru ∼ 1:1, 78 wt % on carbon, Tanaka Kikinzoku) was employed as a reference. $Co_{88}Pt_6Ru_6/NC$ has a large geometric current density of 15.96 mA cm^{-2} at 0.7 V_{RHE}, which is 4.7 times greater than that of PtRu/C at the same potential (3.38 mA cm^{-2}) (Figures 3g and S26). After normalization, the specific (Figure S27) and mass activities of $Co_{88}Pt_6Ru_6/NC$ were both still about 4 times higher than those of PtRu/C (Figure S28). Utilizing CA measurements is a more rational approach for assessing catalyst activity at steady-state conditions, especially for DMFC applications. In contrast to commercial PtRu/C, which does not show MOR activity until 0.4 V_{RHE}, $Co_{88}Pt_6Ru_6/NC$ showed oxidative current as low as 0.3 V_{RHE} (Figure 3h). The CA results of specific and mass activity under other potentials from 0.4−0.7 V_{RHE} were also compared, as shown in Figures 3i and S29, where $Co_{88}Pt_6Ru_6/NC$ exhibited higher activity under all applied potentials. The specific and mass activities at 0.5, 0.6, and 0.7 V_{RHE} were averaged with the standard deviation taken as error bars across three independent measurements (Figure S30), which were all several times higher than those of the commercial PtRu/C catalyst. Particularly, the high specific activity (2.1 ± 0.2 mA cm_{Pt}^{-2}) and mass activity (0.28 ± 0.06 A mg_{Pt+Ru}^{-1}) of $Co_{88}Pt_6Ru_6/NC$ at 0.6 V_{RHE} is 4.4 and 3.9 times higher compared to those of commercial PtRu/C (0.48 mA cm_{Pt}^{-2} and 0.072 A mg_{Pt+Ru}^{-1}), respectively (Figure 3j and Table S1).

Acid Treatment of $Co_{88}Pt_6Ru_6/NC$. The acid stability of $Co_{88}Pt_6Ru_6/NC$ was investigated, as many catalysts can be gradually transformed in an acidic electrolyte or under electrochemical conditions.[51] $Co_{88}Pt_6Ru_6/NC$ after MOR measurements were reserved (approximately 5 h of testing

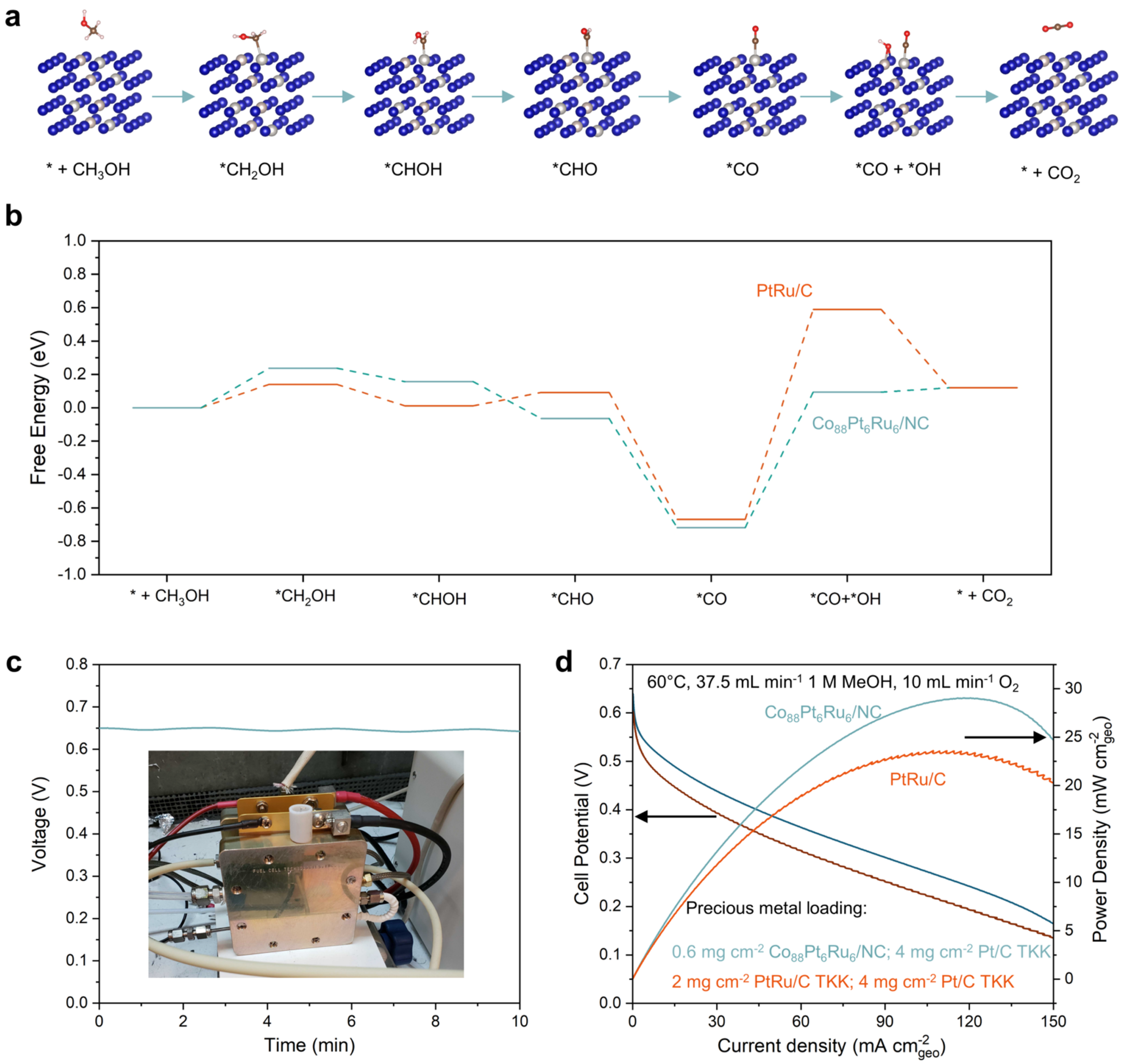

Figure 5. DFT calculations and DMFCs. (a) Reaction pathway for the MOR of Co−Pt−Ru. (b) Free energy diagram of the MOR for $Co_{88}Pt_6Ru_6$/NC and PtRu/C at 0 V. (c) OCV curve for $Co_{88}Pt_6Ru_6$/NC; inset is a digital photo for DMFCs. (d) Comparison of DMFC performance of $Co_{88}Pt_6Ru_6$/NC and PtRu/C catalysts at the anode with 1 M methanol at 60 °C.

time) and then investigated by STEM. The solid nanoparticles appeared to have been etched by acid to form a porous network structure. EDX mapping revealed that Co remained in the structure and all elements continued to be homogeneously distributed (Figure S31).

To understand the acid stability of $Co_{88}Pt_6Ru_6$/NC, acid treatment was carried out by immersing the pristine material in 0.1 M $HClO_4$ for 24, 72, and 200 h. From the XRD results (Figure 4a), most of the *fcc*-Co structures were dissolved, as the peak at 44.2° exhibited a notable reduction in intensity while the *hcp*-Co structure peak positions were almost unchanged. The predominant peak around 44° was split into two peaks corresponding to fcc-Co and hcp-Co. The XPS peaks in the Co 2p energy range of the catalysts after acid treatment could be deconvoluted into only two peaks instead of the three peaks found in the pristine material (Figure 4b). The peaks around 778 and 793 eV, corresponding to Co^0, disappeared while the peak around 781 eV (similar to that reported for a PtCo alloy[52]) remained, suggesting that while Co was dissolved, the Co alloyed with Pt and/or Ru was more stable.[53] No significant change of the XPS spectra for the Pt 4f region (Figure S32a) was observed, whereas the peak for Ru $3p_{3/2}$ was shifted to higher binding energies (Figure S32b), which might be explained by Co^0 providing charge transfer to Ru or Ru−O formed during acid treatment.[54] Using STEM, the microporous structure was clearly observed after 24 h of acid treatment (Figure 4c). One nanoparticle in an intermediate state of dissolution was imaged (Figure 4d), where some of the Co was dissolved to form a porous structure and some remained solid. The mapping results showed that the porous part was Pt-rich, while the solid part was Co-rich (Figure 4e−g). Pt showed stronger intensity after Co was dissolved, indicating that the previously Pt-poor phase lost Co and became porous while the Pt-rich phase almost retained full density, which further supports that the alloying effect of Ru and Pt can make Co more stable in acidic conditions. EDX mapping also revealed homogeneous distributions of Co, Pt, and Ru in the nanoparticles after they were fully etched (Figure S33). The ICP-OES results showed that the relative atomic percentage of Co in the nanoparticles decreased while those of Pt and Ru increased after 24 h of acid treatment (Figures 4h and S34). The metal atomic percentages of $Co_{88}Pt_6Ru_6$/NC_24h are 48.1% for Co, 29.6% for Pt, and 22.3% for Ru, which are close to the EDX results for $Co_{88}Pt_6Ru_6$/NC after MOR measurements and acid treatment. However, a longer acid treatment did not alter the ratio among these three elements ($Co_{44.7}Pt_{29.9}Ru_{25.4}$ for 72 h and $Co_{46.5}Pt_{29.1}Ru_{24.4}$ for 200 h), indicating the adoption of a, at least, seemingly metastable structure after partial dissolution in the acid electrolyte.

The MOR activities of the acid-soaked samples were measured to assess the effects of dissolution on electrochemical activity, as shown in Figure S35. The CV curves exhibited similarity across geometric, specific, and mass activities, which is reasonable considering that the metal compositions of the nanoparticles are almost the same. Although the activity is lower than that of pristine $Co_{88}Pt_6Ru_6$/NC, the activities of all acid-treated materials are still higher than that of commercial PtRu/C catalysts and most reported catalysts (Table S1). From the CA measurements (Figures S36 and S37), the specific activity and mass activity of acid-treated samples are slightly lower than those of the samples before acid treatment but much higher than those of the commercial PtRu/C. The currents of the acid-treated samples at 10 min under 0.5 and 0.6 V_{RHE} were selected for comparison, as displayed in Figures 4i and 5j. The specific activities of $Co_{88}Pt_6Ru_6$/NC, $Co_{88}Pt_6Ru_6$/NC_24h, $Co_{88}Pt_6Ru_6$/NC_72h, $Co_{88}Pt_6Ru$/NC_200h were measured to be 20.3, 15.6, 14.1, 14.4, and 7.0 mA cm_{Pt}^{-2} at 0.5 V_{RHE}, respectively, and were all at least twice higher compared to PtRu/C, demonstrating the excellent activity and suitability for DMFCs application. The slight decay in the performance might be ascribed to the dissolution of Co in the nanoparticles in the acidic environment, which probably serves as an auxiliary component that regulates the electronic structure of the active sites without being catalytically active.

Mechanism Studies and DMFCs. To understand the role of each component within the system, control experiments were conducted to decouple the interactions between the various metal constituents. Co NPs/NC and $Co_{94}Ru_6$/NC showed no MOR activity below 1.0 V_{RHE} (Figure S38), as expected from the lack of Pt incorporation. $Co_{94}Pt_6$/NC has a similar onset potential but a higher MOR current density compared to that of commercial Pt/C (TKK, 46 wt %) (Figure S39). We therefore conclude that Pt is the active site for the MOR, and Ru acts to facilitate *CO removal. ZIF-8 was also employed as a precursor to understand the effects of Co. Pure nitrogen-doped carbon was obtained (Figure S40a) because the Zn (boiling point of 907 °C) in ZIF-8 was evaporated during the first pyrolysis process at 1000 °C.[46] Afterward, the same amount of Pt and Ru precursors were added, which was followed by the second pyrolysis. The XRD results indicate that no Pt or Ru nanoparticles were formed. Furthermore, the flat cyclic voltammogram of Pt−Ru/NC shows the absence of methanol oxidation. As the ICP-OES results showed only less than 1% Pt and Ru in the composite material, Co also appears to be an important support for loading Pt^{4+} and Ru^{3+} ions on the material prior to the second thermal annealing (Figure S40).

Figure 5a displays the reaction pathway of the MOR on Co−Pt−Ru(001), which was used to simulate the structure of the most active composition, $Co_{88}Pt_6Ru_6$/NC. The $*CH_2OH$, *CHOH, *CHO, and *CO intermediates were formed as CH_3OH was progressively dehydrogenated on the Pt site. Then, *OH was formed on the Ru site near Pt by water dissociation and reacted with *CO to yield CO_2. The reaction pathway is the same as that on the PtRu(111) surface (Figure S41). The free energy diagrams for the MOR reaction pathway on the Co−Pt−Ru(001) and PtRu(111) surfaces were calculated to determine the origin of the improved performance at a potential of 0 V_{RHE} (Figure 5b). The elementary step energetics of the first four steps display similar energy changes for both surfaces. For Co−Pt−Ru(001), after the first deprotonation process, the overall formation of *CO is downhill in energy. While the RDS step for both surfaces is *OH formation (from *CO to *CO + *OH), the activation barrier on Co−Pt−Ru(001) (0.81 eV) is about 0.45 eV lower than that on and PtRu(111) (1.26 eV). As such, it is clear that $Co_{88}Pt_6Ru_6$/NC can effectively lower the energy barrier for CO oxidation and facilitate CO removal, suggesting that the $Co_{88}Pt_6Ru_6$/NC catalyst is resilient to CO poisoning. CO stripping was carried out to further demonstrate this point (Figure S42). $Co_{88}Pt_6Ru_6$/NC exhibited a higher stripping current at 0.5 V_{RHE}, which is consistent with the higher current density during the MOR. Also, $Co_{88}Pt_6Ru_6$/NC had a lower onset potential for CO stripping than commercial PtRu/C, supporting the DFT calculations and explaining why $Co_{88}Pt_6Ru_6$/NC could deliver comparable MOR activity at lower potentials. Commercial PtRu/C displays a prolonged current tail, indicating heightened susceptibility to CO poisoning on the Pt sites. However, the sharp peak of $Co_{88}Pt_6Ru_6$/NC suggests more facile *CO removal on its surface and more available sites for further reactions. Combined with the DFT and CO stripping results, $Co_{88}Pt_6Ru_6$/NC appears to be more resilient to CO poisoning and has a lower energy barrier for the RDS of the MOR, explaining the high MOR activity measured.

Motivated by the impressive MOR performance of the optimized $Co_{88}Pt_6Ru_6$/NC, a direct methanol fuel cell employing $Co_{88}Pt_6Ru_6$/NC catalysts as the anode and commercial Pt/C catalysts as the cathode was constructed to reflect practical applications. The open-circuit voltage of the device was stable at 0.65 V (Figure 5c). Despite a lower loading, the DMFCs driven by $Co_{88}Pt_6Ru_6$/NC could deliver a higher peak power density of 28 ± 1 mW cm^{-2} (Figures 5d and S43) compared to DMFCs driven by commercial PtRu/C (23.6 mW cm^{-2}), giving 4.1 times higher power density if normalized by the noble metal loading. Also, its performance was compared with that of other reported DMFCs (Table S2). Although the geometric activity is lower than that of some optimized devices with different loading and operation conditions, the mass activity of our DMFCs (48.3 mW mg_{Pt+Ru}^{-1}) is comparable or even higher. Further, the long-term stability of $Co_{88}Pt_6Ru_6$/NC was measured using a three-electrode system (Figure S44) and DMFC (Figure S45). The current decreased by around 70% after 10 h of measurement and was stabilized for more than 30 h in a three-electrode system, which was mainly due to the accumulation of poisoning species such as CO on the catalyst surface over a long period of time, leading to the inactivation of the active sites and the continuous volatilization of methanol during the test. However, the stability is still better than that of the most reported MOR catalysts as they suffer more than 70% current drop within 1 h. On the other hand, the current only showed a ∼35% decrease after 48 h of operation in the DMFC. The better stability in DMFC might be attributed to the fact that flow can remove some of the poisonous species. Although the stability of the MOR has always been a thorny issue, we believe that it can be improved through further engineering adjustments.

■ CONCLUSIONS

We comprehensively investigate the use of the Co−Pt−Ru system for methanol oxidation. DFT calculations reveal that Co not only weakens *CO adsorption but facilitates the *OH formation as well. The RDS of the MOR is from *CO to *CO + *OH, and $Co_{88}Pt_6Ru_6$/NC can effectively lower the energy barrier for the RDS. The Pt loading can be tuned by changing the amount of the precursor. At 0.6 V_{RHE}, $Co_{88}Pt_6Ru_6$/NC has both high specific activity of 2.1 ± 0.2 mA cm_{Pt}^{-2} and mass activity of 0.28 ± 0.06 A mg_{Pt+Ru}^{-1}, which are both approximately 4 times higher than the same respective metrics of commercial PtRu/C. Furthermore, the transformation of catalysts in acid conditions revealed that part of the Co can be dissolved in an acidic solution and the solid nanoparticles transform into a (meta)stable porous network structure with a homogeneous distribution of Co, Pt, and Ru. The MOR activity of $Co_{88}Pt_6Ru_6$/NC after acid treatment was still superior to that of PtRu/C. DMFCs were assembled to fully demonstrate the catalytic performance of $Co_{88}Pt_6Ru_6$/NC, which can reach a peak power density of 28 ± 1 mW cm^{-2}, which is 4.1 times that of the commercial PtRu/C catalysts normalized by precious metal loading. For further research, several aspects can be investigated, such as improving the size uniformity of the nanoparticles and finding other transition metals that can regulate the binding energy but are more acid-resistant to support Pt and Ru. Moreover, improving the stability of Co−Pt−Ru/NC and other MOR catalysts is important for practical applications. Our findings demonstrate the clear advantage of using abundant support that, while not necessarily electroactive, changes the electronic structure of electroactive components while simultaneously maximizing their utilization, thereby providing potential new design approaches for the MOR and other electrocatalysts for DMFCs and beyond.

■ METHODS

Synthesis of Co−Pt−Ru/NC. All chemicals were used as received without further purification. Milli-Q deionized water was used in all experiments. First, ZIF-67 was prepared by a precipitation reaction between $Co(NO_3)_2 \cdot 6H_2O$ (1.23 g) and 2-methylimidazole (1.46 g) in 50 mL methanol at ambient conditions. After 20 h of reaction, ZIF-67 was obtained by centrifugation and then washed with methanol 3 times, followed by drying in the oven overnight. To prepare Co NPs/NC, an alumina boat crucible loaded with ZIF-67 was placed in a tube furnace, heated to 1000 °C at a rate of 5 °C min^{-1}, and then maintained at that temperature for 2 h under N_2 flow. After that, 100 mg of Co NPs/NC was dispersed in 50 mL H_2O and sonicated for 30 min. 5 mL of $H_2PtCl_6 \cdot xH_2O$ (4 mg mL^{-1}) and 5 mL of $RuCl_3 \cdot xH_2O$ (4 mg mL^{-1}) were added to the suspension and stirred for 2 h. The suspension was centrifuged 3 times with water and dried overnight to obtain Co + Pt + Ru/NC. The final product, Co−Pt−Ru/NC, was prepared by the pyrolysis of Co + Pt + Ru/NC at 900 °C at a rate of 5 °C min^{-1} for 2 h under N_2 flow.

To explore the pyrolysis conditions, the temperature and dwelling time were varied. Co + Pt + Ru/NC was pyrolyzed at 300 °C for 10 min, 1 h, and 2 h, 600 °C for 10 min, 1 h, and 2 h, and 900 °C for 10 min, 1 h, and 2 h. The Pt loading in Co−Pt−Ru/NC was regulated by adding different amounts of the Pt precursor. Typically, the amount of Co NPs/NC and $RuCl_3 \cdot xH_2O$ were kept the same, and 1.25, 2.5, 4, 12.5, and 25 mL $H_2PtCl_6 \cdot xH_2O$ (4 mg mL^{-1}) were added. The final products were named as $Co_{93}Pt_1Ru_6$/NC, $Co_{91}Pt_3Ru_6$/NC, $Co_{88}Pt_6Ru_6$/NC, $Co_{74}Pt_{20}Ru_6$/NC, and $Co_{54}Pt_{40}Ru_6$/NC.

Acid Treatment of $Co_{88}Pt_6Ru_6$/NC. To mimic the electrolyte environment, 0.1 M $HClO_4$ was used for acid treatment of $Co_{88}Pt_6Ru_6$/NC. Generally, 50 mg of $Co_{88}Pt_6Ru_6$/NC was dispersed in 50 mL of 0.1 M $HClO_4$ for 24, 72, and 200 h. After centrifugation 3 times with H_2O and drying overnight, the samples after acid treatment were obtained and named as $Co_{88}Pt_6Ru_6$/NC_24h, $Co_{88}Pt_6Ru_6$/NC_72h, and $Co_{88}Pt_6Ru_6$/NC_200h.

Material Characterization. Powder X-ray diffraction (XRD) was carried out with a Bruker D2 Phaser Gen II X-ray powder diffractometer equipped with a Cu-sealed tube (wavelength λ = 1.5418 Å) at 30 kV and 10 mA. The metal weight and atomic percentages of the samples were determined by inductively coupled plasma optical emission spectroscopy (ICP-OES) with an Agilent 5100 DVD inductively coupled plasma optical emission spectrometer. To analyze the morphology of the precursors and products, Zeiss Merlin high-resolution scanning electron microscope (SEM) was used. High-angle annular dark-field scanning transmission electron microscopy (HAADF-STEM) imaging was conducted using a probe-aberration-corrected Thermo Fisher Scientific Themis Z G3 60−300 kV S/TEM at 200 kV. Energy-dispersive X-ray (EDX) mapping data were collected using a Thermo Fisher Scientific Super-X detector. The elemental chemical states of the as-prepared products were determined by X-ray photoelectron spectroscopy (XPS) with a Thermo Scientific K-α+ spectrometer using monochromatic Al Kα radiation (1,486.6 eV). The binding energy of the C 1s peak at 284.6 eV was used as the reference.

Electrochemical Measurements. Electrodes were prepared by drop-casting the ink containing the catalyst powder with Nafion on a glassy carbon (GC) disk electrode (Pine Research, 5 mm diameter). Typically, 5 mg of the catalyst was dispersed in a mixture of 980 μL ethanol and 20 μL Nafion (5 wt %) via ultrasonication for 60 min to form the catalyst ink. 10 μL of the catalyst ink was dropped onto the GC with a nominal loading of 250 $\mu g_{catalyst}$ cm_{geo}^{-2} and 46 μg_{Nafion} cm_{geo}^{-2}. Electrochemical measurements were carried out in a three-electrode setup in a glass electrochemical cell with an Ag/AgCl reference electrode and a carbon rod counter electrode. The Ag/AgCl reference electrode was calibrated in the same electrolyte by measuring hydrogen oxidation/evolution using a platinum working electrode and defining the point of zero current as 0 V vs RHE. The potential was controlled using a Biologic VSP-300 potentiostat. Cyclic voltammetry (CV) was performed in a solution of Ar-saturated 1 M CH_3OH in 0.1 M $HClO_4$ with a potential range of ∼0.05−1.2 V vs RHE at a scan rate of 50 mV/s. The background current was collected from the CV of the catalysts in Ar-saturated 0.1 M $HClO_4$ before CH_3OH addition. Chronoamperometry (CA) measurements were recorded from 0.3−0.7 V vs RHE with a 0.1 V interval. The ohmic losses were corrected by subtracting the ohmic drop from the measured potential using the electrolyte resistance. The potential after iR correction was calculated using $E_{RHE} = 0.263\text{ V} + E_{tested} - iR$. More details are provided in the Supporting Information.

CO Stripping Experiments. The CO stripping activities of Co−Pt−Ru/NC and PtRu/C were compared. Typically, after surface cleaning (0.1 M $HClO_4$), the catalysts were subjected to CO adsorption at 0.05 V vs RHE for 30 min and the solution was then purged with Ar to remove unbound CO. The stripping data were collected using CV at a scan rate of 10 mV/s. The current was corrected using the background current.

DMFC Measurements. The as-synthesized $Co_{88}Pt_6Ru_6$/NC and commercial Pt/C (67%, Tanaka Kikinzoku, "TKK") were used as catalysts at the anode and cathode to fabricate the membrane electrode assembly (MEA), respectively. First, 40 mg of the catalyst powder was dispersed in 2 mL isopropanol alcohol (IPA) with 200 μL Nafion (5 wt %) and sonicated for 1 h. The catalyst was drop-cast onto carbon cloth to reach a loading of 6 mg cm^{-2} for $Co_{88}Pt_6Ru_6$/NC and a precious metal loading of 4 mg_{Pt} cm^{-2} for Pt/C as the anode and cathode, respectively. The MEAs were fabricated by sandwiching the Nafion 117 membrane between the anode and cathode, followed by hot pressing at 120 °C under a pressure of 0.2 MPa for 3 min. The assembled DMFC was tested at 60 °C by feeding 1 M CH_3OH at the anode at a flow rate of 37.5 mL min^{-1} and feeding dry oxygen at the cathode at a flow rate of 10 mL min^{-1}. The open-circuit potential was measured first, and linear sweep voltammetry (LSV) was conducted to measure the polarization curves at a scan rate of 10 mV s^{-1}. Commercial PtRu/C (78%, TKK) was used for comparison by replacing $Co_{88}Pt_6Ru_6$/NC with PtRu/C with a precious metal loading of 2 mg_{PtRu} cm^{-2}.

DFT Calculations. Spin-polarized density functional theory (DFT) calculations were performed with the Vienna ab initio simulation package (VASP) using the projector-augmented plane wave method with a cutoff of 450 eV. The Ru_pv pseudopotential was employed for ruthenium, where semicore p states were treated as valence states. Exchange correlation was applied in the Perdew, Burke, and Ernzerhof functional within a generalized gradient approximation (GGA-PBE). The Pt(111) and Ru(0001) surfaces were cleaved from the relaxed bulk material. The Pt(111) and Ru(0001) slabs were constructed as 2 × 2 periodic supercells containing six atomic layers, where the bottom three layers were fixed with vacuum separation >10 Å in the *Z*-direction and γ-centered **k**-point sampling of 4 × 4 × 1. The different surface species of methanol electrooxidation ($*CH_2OH$, $*CH_2O$, *CHOH, *CHO, *CO, *OH, $*H_2O$) on the intermetallic structures were placed on one side of the slab. To convert the calculated DFT adsorption energies into Gibbs free energies, the zero point energies and enthalpic and entropic corrections from the vibrational analysis are listed in Table S3. The electronic convergence threshold for the two slabs was 1×10^{-6} eV with a plane wave energy cutoff of 500 eV. In geometric relaxation, all atoms were relaxed with residual forces smaller than 0.01 eV $Å^{-1}$. For PtRu(111)[25] and cobalt intermetallic $Co_3Pt(001)$, $Co_3Ru(001)$, and CoPtRu(001), a 4-layer slab of 2 × 2 periodic supercells with the bottom two layers was fixed and vacuum-separated >10 Å in the *z*-direction. The structure converges with 2 × 2 × 1 K-point sampling, an electronic convergence threshold of 1×10^{-6} eV, a plane wave energy cutoff of 450 eV, and a residual force threshold of 0.01 eV $Å^{-1}$. For all metallic and intermetallic structures, a Gaussian smearing of 0.1 eV was used. The gas-phase species (H_2, H_2O, CO, and CH_3OH) were computed with a 1 × 1 × 1 **k**-point sampling, electronic convergence threshold of 1×10^{-6} eV, plane wave energy cutoff of 500 eV, and residual forces threshold of 0.01 eV $Å^{-1}$. More details are provided in the Supporting Information.

■ ASSOCIATED CONTENT

Supporting Information

The Supporting Information is available free of charge at https://pubs.acs.org/doi/10.1021/acs.chemmater.4c01008.

> Experimental methods: synthesis; electrochemical methods and protocols; DFT calculations; free energy diagrams and corresponding structures; PXRD patterns; SEM; ICP-OES; HAADF-STEM; EDX; electrochemical characterization; CO stripping; comparison of MEA performance (PDF)

■ AUTHOR INFORMATION

Corresponding Authors

Yuriy Román-Leshkov − *Department of Chemical Engineering, Massachusetts Institute of Technology, Cambridge, Massachusetts 02139, United States;* orcid.org/0000-0002-0025-4233; Email: yroman@mit.edu

Ju Li − *Department of Materials Science and Engineering, Massachusetts Institute of Technology, Cambridge, Massachusetts 02139, United States; Department of Nuclear Science and Engineering, Massachusetts Institute of Technology, Cambridge, Massachusetts 02139, United States;* orcid.org/0000-0002-7841-8058; Email: liju@mit.edu

Authors

Hongbin Xu − *Department of Materials Science and Engineering, Massachusetts Institute of Technology, Cambridge, Massachusetts 02139, United States;* orcid.org/0009-0007-6311-475X

Daniel J. Zheng − *Department of Materials Science and Engineering, Massachusetts Institute of Technology, Cambridge, Massachusetts 02139, United States;* orcid.org/0000-0002-9471-6856

Haldrian Iriawan − *Department of Materials Science and Engineering, Massachusetts Institute of Technology, Cambridge, Massachusetts 02139, United States;* orcid.org/0000-0002-2997-1180

Jen-Hung Fang − *Research Laboratory of Electronics, Massachusetts Institute of Technology, Cambridge, Massachusetts 02139, United States;* orcid.org/0000-0001-8665-4088

Junghwa Kim − *Department of Materials Science and Engineering, Massachusetts Institute of Technology, Cambridge, Massachusetts 02139, United States; Research Laboratory of Electronics, Massachusetts Institute of Technology, Cambridge, Massachusetts 02139, United States*

Xiao Wang − *Department of Chemical Engineering, Massachusetts Institute of Technology, Cambridge, Massachusetts 02139, United States;* orcid.org/0000-0003-1624-8230

Yang Shao-Horn − *Department of Materials Science and Engineering, Massachusetts Institute of Technology, Cambridge, Massachusetts 02139, United States; Research Laboratory of Electronics and Department of Mechanical Engineering, Massachusetts Institute of Technology, Cambridge, Massachusetts 02139, United States;* orcid.org/0000-0001-8714-2121

Complete contact information is available at: https://pubs.acs.org/10.1021/acs.chemmater.4c01008

Author Contributions

[#]H.X. and D.Z. contributed equally to this work. J.L., Y.R.-L., and H.X. conceived the original idea. H.X. performed the synthesis, the electrochemical measurements, and data analysis with assistance from D.J.Z. H.X. performed characterization and analysis. J.H.F. and H.X. performed DMFC measurements. J.K. and H.X. performed STEM. H.I. and H.X. conducted DFT calculations. H.X., Y.S.-H., J.L., and Y.R.-L., drafted the manuscript. All authors contributed to the revision of the manuscript.

Notes

The authors declare no competing financial interest.

■ ACKNOWLEDGMENTS

This work was supported by the Eni S.p.A. through the MIT Energy Initiative. We thank Zhichu Ren, Sunmoon Yu, Botao Huang, Bryce Tappan, and Daniel Wang for their discussion. This work used the Materials Research Laboratory Shared Experimental Facilities at Massachusetts Institute of Technology. This work was carried out in part through the use of MIT.nano's facilities, and in part at the Center for Nanoscale Systems of Harvard University.

■ REFERENCES

(1) Wu, Y.; Jiang, Z.; Lu, X.; Liang, Y.; Wang, H. Domino Electroreduction of CO2 to Methanol on a Molecular Catalyst. *Nature* **2019**, *575* (7784), 639−642.

(2) Yang, H.; Wu, Y.; Li, G.; Lin, Q.; Hu, Q.; Zhang, Q.; Liu, J.; He, C. Scalable Production of Efficient Single-Atom Copper Decorated Carbon Membranes for CO$_2$ Electroreduction to Methanol. *J. Am. Chem. Soc.* **2019**, *141* (32), 12717−12723.

(3) Bagchi, D.; Raj, J.; Singh, A. K.; Cherevotan, A.; Roy, S.; Manoj, K. S.; Vinod, C. P.; Peter, S. C. Structure-Tailored Surface Oxide on Cu−Ga Intermetallics Enhances CO$_2$ Reduction Selectivity to Methanol at Ultralow Potential. *Adv. Mater.* **2022**, *34* (19), No. 2109426.

(4) Kong, S.; Lv, X.; Wang, X.; Liu, Z.; Li, Z.; Jia, B.; Sun, D.; Yang, C.; Liu, L.; Guan, A.; Wang, J.; Zheng, G.; Huang, F. Delocalization State-Induced Selective Bond Breaking for Efficient Methanol Electrosynthesis from CO2. *Nat. Catal.* **2023**, *6* (1), 6−15.

(5) Feng, Y.; Liu, H.; Yang, J. A Selective Electrocatalyst−Based Direct Methanol Fuel Cell Operated at High Concentrations of Methanol. *Sci. Adv.* **2017**, *3* (6), No. e1700580.

(6) Mehmood, A.; Scibioh, M. A.; Prabhuram, J.; An, M.-G.; Ha, H. Y. A Review on Durability Issues and Restoration Techniques in Long-Term Operations of Direct Methanol Fuel Cells. *J. Power Sources* **2015**, *297*, 224−241.

(7) Li, J.; Wei, R.; Wang, X.; Zuo, Y.; Han, X.; Arbiol, J.; Llorca, J.; Yang, Y.; Cabot, A.; Cui, C. Selective Methanol-to-Formate Electrocatalytic Conversion on Branched Nickel Carbide. *Angew. Chem., Int. Ed.* **2020**, *59* (47), 20826−20830.

(8) Wang, J.; Zhang, B.; Guo, W.; Wang, L.; Chen, J.; Pan, H.; Sun, W. Toward Electrocatalytic Methanol Oxidation Reaction: Long-standing Debates and Emerging Catalysts. *Adv. Mater.* **2023**, *35*, No. 2211099.

(9) Lai, S. C. S.; Lebedeva, N. P.; Housmans, T. H. M.; Koper, M. T. M. Mechanisms of Carbon Monoxide and Methanol Oxidation at Single-Crystal Electrodes. *Top. Catal.* **2007**, *46* (3−4), 320−333.

(10) Katayama, Y.; Kubota, R.; Rao, R. R.; Hwang, J.; Giordano, L.; Morinaga, A.; Okanishi, T.; Muroyama, H.; Matsui, T.; Shao-Horn, Y.; Eguchi, K. Direct Observation of Surface-Bound Intermediates During Methanol Oxidation on Platinum Under Alkaline Conditions. *J. Phys. Chem. C* **2021**, *125* (48), 26321−26331.

(11) Yang, C.; Jiang, Q.; Li, W.; He, H.; Yang, L.; Lu, Z.; Huang, H. Ultrafine Pt Nanoparticle-Decorated 3D Hybrid Architectures Built from Reduced Graphene Oxide and MXene Nanosheets for Methanol Oxidation. *Chem. Mater.* **2019**, *31* (22), 9277−9287.

(12) Yao, W.; Jiang, X.; Li, M.; Li, Y.; Liu, Y.; Zhan, X.; Fu, G.; Tang, Y. Engineering Hollow Porous Platinum-Silver Double-Shelled Nanocages for Efficient Electro-Oxidation of Methanol. *Appl. Catal., B* **2021**, *282*, No. 119595.

(13) Li, Z.; Jiang, X.; Wang, X.; Hu, J.; Liu, Y.; Fu, G.; Tang, Y. Concave PtCo Nanocrosses for Methanol Oxidation Reaction. *Appl. Catal., B* **2020**, *277*, No. 119135.

(14) Gong, L.; Yang, Z.; Li, K.; Xing, W.; Liu, C.; Ge, J. Recent Development of Methanol Electrooxidation Catalysts for Direct Methanol Fuel Cell. *J. Energy Chem.* **2018**, *27* (6), 1618−1628.

(15) Lu, X.; Deng, Z.; Guo, C.; Wang, W.; Wei, S.; Ng, S.-P.; Chen, X.; Ding, N.; Guo, W.; Wu, C.-M. L. Methanol Oxidation on Pt$_3$Sn(111) for Direct Methanol Fuel Cells: Methanol Decomposition. *ACS Appl. Mater. Interfaces* **2016**, *8* (19), 12194−12204.

(16) Prabhuram, J.; Zhao, T. S.; Liang, Z. X.; Chen, R. A Simple Method for the Synthesis of PtRu Nanoparticles on the Multi-Walled Carbon Nanotube for the Anode of a DMFC. *Electrochim. Acta* **2007**, *52* (7), 2649−2656.

(17) Candelaria, S. L.; Bedford, N. M.; Woehl, T. J.; Rentz, N. S.; Showalter, A. R.; Pylypenko, S.; Bunker, B. A.; Lee, S.; Reinhart, B.; Ren, Y.; Ertem, S. P.; Coughlin, E. B.; Sather, N. A.; Horan, J. L.; Herring, A. M.; Greenlee, L. F. Multi-Component Fe−Ni Hydroxide Nanocatalyst for Oxygen Evolution and Methanol Oxidation Reactions under Alkaline Conditions. *ACS Catal.* **2017**, *7* (1), 365−379.

(18) Dubale, A. A.; Zheng, Y.; Wang, H.; Hübner, R.; Li, Y.; Yang, J.; Zhang, J.; Sethi, N. K.; He, L.; Zheng, Z.; Liu, W. High-Performance Bismuth-Doped Nickel Aerogel Electrocatalyst for the Methanol Oxidation Reaction. *Angew. Chem., Int. Ed.* **2020**, *59* (33), 13891−13899.

(19) Shi, X.; Iqbal, N.; Kunwar, S. S.; Wahab, G.; Kasat, H. A.; Kannan, A. M. Pt Co@NCNTs Cathode Catalyst Using ZIF-67 for Proton Exchange Membrane Fuel Cell. *Int. J. Hydrogen Energy* **2018**, *43* (6), 3520−3526.

(20) Anwar, R.; Iqbal, N.; Hanif, S.; Noor, T.; Shi, X.; Zaman, N.; Haider, D.; Rizvi, S. A. M.; Kannan, A. M. MOF-Derived CuPt/NC Electrocatalyst for Oxygen Reduction Reaction. *Catalysts* **2020**, *10* (7), No. 799.

(21) Khan, S.; Noor, T.; Iqbal, N.; Pervaiz, E. Recent Advancement in Metal-Organic Framework for Water Electrolysis: A Review. *ChemNanoMat* **2022**, *8*, No. e202200115.

(22) Asif, U. A.; Noor, T.; Pervaiz, E.; Iqbal, N.; Zaman, N. LSTN ($\mathrm{La0_{.4}Sr_{0.4}Ti_{0.9}Ni_{0.1}O_{3\text{-}\&}}$) perovskite and graphitic carbon nitride (g-C_3N_4) hybrids as a bifunctional electrocatalyst for water-splitting applications. *J. Alloys Compd.* **2023**, *939*, No. 168668.

(23) Gojković, S.; Vidaković, T. R.; Đurović, D. R. Kinetic Study of Methanol Oxidation on Carbon-Supported PtRu Electrocatalyst. *Electrochim. Acta* **2003**, *48* (24), 3607−3614.

(24) Iwasita, T.; Hoster, H.; John-Anacker, A.; Lin, W. F.; Vielstich, W. Methanol Oxidation on PtRu Electrodes. Influence of Surface Structure and Pt−Ru Atom Distribution. *Langmuir* **2000**, *16* (2), 522−529.

(25) Tripković, A.; Popović, K. D.; Grgur, B. N.; Blizanac, B.; Ross, P. N.; Marković, N. M. Methanol Electrooxidation on Supported Pt and PtRu Catalysts in Acid and Alkaline Solutions. *Electrochim. Acta* **2002**, *47* (22−23), 3707−3714.

(26) Lee, S. W.; Chen, S.; Sheng, W.; Yabuuchi, N.; Kim, Y.-T.; Mitani, T.; Vescovo, E.; Shao-Horn, Y. Roles of Surface Steps on Pt Nanoparticles in Electro-Oxidation of Carbon Monoxide and Methanol. *J. Am. Chem. Soc.* **2009**, *131* (43), 15669−15677.

(27) Suntivich, J.; Xu, Z.; Carlton, C. E.; Kim, J.; Han, B.; Lee, S. W.; Bonnet, N.; Marzari, N.; Allard, L. F.; Gasteiger, H. A.; Hamad-Schifferli, K.; Shao-Horn, Y. Surface Composition Tuning of Au−Pt Bimetallic Nanoparticles for Enhanced Carbon Monoxide and Methanol Electro-Oxidation. *J. Am. Chem. Soc.* **2013**, *135* (21), 7985−7991.

(28) Guo, J. W.; Zhao, T. S.; Prabhuram, J.; Chen, R.; Wong, C. W. Preparation and Characterization of a PtRu/C Nanocatalyst for Direct Methanol Fuel Cells. *Electrochim. Acta* **2005**, *51* (4), 754−763.

(29) Long, J. W.; Stroud, R. M.; Swider-Lyons, K. E.; Rolison, D. R. How To Make Electrocatalysts More Active for Direct Methanol OxidationAvoid PtRu Bimetallic Alloys! *J. Phys. Chem. B* **2000**, *104* (42), 9772−9776.

(30) Noor, T.; Mohtashim, M.; Iqbal, N.; Naqvi, S. R.; Zaman, N.; Rasheed, L.; Yousuf, M. Graphene Based FeO/NiO MOF Composites for Methanol Oxidation Reaction. *J. Electroanal. Chem.* **2021**, *890*, No. 115249.

(31) Tritsaris, G. A.; Rossmeisl, J. Methanol Oxidation on Model Elemental and Bimetallic Transition Metal Surfaces. *J. Phys. Chem. C* **2012**, *116* (22), 11980−11986.

(32) Casado-Rivera, E.; Volpe, D. J.; Alden, L.; Lind, C.; Downie, C.; Vázquez-Alvarez, T.; Angelo, A. C. D.; DiSalvo, F. J.; Abruña, H. D. Electrocatalytic Activity of Ordered Intermetallic Phases for Fuel Cell Applications. *J. Am. Chem. Soc.* **2004**, *126* (12), 4043−4049.

(33) Chen, Q.; Yang, Y.; Cao, Z.; Kuang, Q.; Du, G.; Jiang, Y.; Xie, Z.; Zheng, L. Excavated Cubic Platinum−Tin Alloy Nanocrystals Constructed from Ultrathin Nanosheets with Enhanced Electrocatalytic Activity. *Angew. Chem. Int. Ed* **2016**, *55* (31), 9021−9025.

(34) Haner, A. N.; Ross, P. N. Electrochemical Oxidation of Methanol on Tin-Modified Platinum Single-Crystal Surfaces. *J. Phys. Chem. A* **1991**, *95* (9), 3740−3746.

(35) Chen, L.; Liang, X.; Wang, D.; Yang, Z.; He, C.-T.; Zhao, W.; Pei, J.; Xue, Y. Platinum−Ruthenium Single Atom Alloy as a Bifunctional Electrocatalyst toward Methanol and Hydrogen Oxidation Reactions. *ACS Appl. Mater. Interfaces* **2022**, *14* (24), 27814−27822.

(36) Poerwoprajitno, A. R.; Gloag, L.; Watt, J.; Cheong, S.; Tan, X.; Lei, H.; Tahini, H. A.; Henson, A.; Subhash, B.; Bedford, N. M.; Miller, B. K.; O'Mara, P. B.; Benedetti, T. M.; Huber, D. L.; Zhang, W.; Smith, S. C.; Gooding, J. J.; Schuhmann, W.; Tilley, R. D. A Single-Pt-Atom-on-Ru-Nanoparticle Electrocatalyst for CO-Resilient Methanol Oxidation. *Nat. Catal.* **2022**, *5* (3), 231−237.

(37) Ma, H.; Zheng, Z.; Zhao, H.; Shen, C.; Chen, H.; Li, H.; Cao, Z.; Kuang, Q.; Lin, H.; Xie, Z. Trimetallic PtNiCo Branched Nanocages as Efficient and Durable Bifunctional Electrocatalysts towards Oxygen Reduction and Methanol Oxidation Reactions. *J. Mater. Chem. A* **2021**, *9* (41), 23444−23450.

(38) Kong, F.; Liu, X.; Song, Y.; Qian, Z.; Li, J.; Zhang, L.; Yin, G.; Wang, J.; Su, D.; Sun, X. Selectively Coupling Ru Single Atoms to PtNi Concavities for High-Performance Methanol Oxidation via *d* -Band Center Regulation. *Angew. Chem. Int. Ed* **2022**, *61* (42), No. e202207524.

(39) Li, J.; Jilani, S. Z.; Lin, H.; Liu, X.; Wei, K.; Jia, Y.; Zhang, P.; Chi, M.; Tong, Y. J.; Xi, Z.; Sun, S. Ternary CoPtAu Nanoparticles as a General Catalyst for Highly Efficient Electro-oxidation of Liquid Fuels. *Angew. Chem., Int. Ed.* **2019**, *58* (33), 11527−11533.

(40) Antolini, E.; Salgado, J. R. C.; Gonzalez, E. R. The Methanol Oxidation Reaction on Platinum Alloys with the First Row Transition Metals. *Appl. Catal., B* **2006**, *63* (1−2), 137−149.

(41) Khalid, W.; Jafar, F.; Iqbal, N.; Ali, Z.; Humayon, A.; Akhtar, J.; Atif, M. Synthesis of Gold-Coated CoFe2O4 and Their Potential in Magnetic Hyperthermia. *Appl. Phys. A* **2018**, *124* (7), No. 501.

(42) Rehman, A. U.; Atif, M.; Younas, M.; Rafique, T.; Wahab, H.; Ul-Hamid, A.; Iqbal, N.; Ali, Z.; Khalid, W.; Nadeem, M. Unusual Semiconductor−Metal−Semiconductor Transitions in Magnetite Fe_3O_4 Nanoparticles. *RSC Adv.* **2022**, *12* (20), 12344−12354.

(43) Nørskov, J. K.; Rossmeisl, J.; Logadottir, A.; Lindqvist, L.; Kitchin, J. R.; Bligaard, T.; Jónsson, H. Origin of the Overpotential for Oxygen Reduction at a Fuel-Cell Cathode. *J. Phys. Chem. B* **2004**, *108* (46), 17886−17892.

(44) Kitchin, J. R.; Nørskov, J. K.; Barteau, M. A.; Chen, J. G. Modification of the Surface Electronic and Chemical Properties of Pt(111) by Subsurface 3d Transition Metals. *J. Chem. Phys.* **2004**, *120* (21), 10240−10246.

(45) Liu, P.; Logadottir, A.; Nørskov, J. K. Modeling the Electro-Oxidation of CO and H_2/CO on Pt, Ru, PtRu and Pt_3Sn. *Electrochim. Acta* **2003**, *48* (25−26), 3731−3742.

(46) Greeley, J.; Nørskov, J. K. Combinatorial Density Functional Theory-Based Screening of Surface Alloys for the Oxygen Reduction Reaction. *J. Phys. Chem. C* **2009**, *113* (12), 4932−4939.

(47) Fernández, E.; Moses, P. G.; Toftelund, A.; Hansen, H. A.; Martínez, J. I.; Abild-Pedersen, F.; Kleis, J.; Hinnemann, B.; Rossmeisl, J.; Bligaard, T.; Nørskov, J. K. Scaling Relationships for Adsorption Energies on Transition Metal Oxide, Sulfide, and Nitride Surfaces. *Angew. Chem. Int. Ed* **2008**, *47* (25), 4683−4686.

(48) Su, J.; Yang, Y.; Xia, G.; Chen, J.; Jiang, P.; Chen, Q. Ruthenium-Cobalt Nanoalloys Encapsulated in Nitrogen-Doped Graphene as Active Electrocatalysts for Producing Hydrogen in Alkaline Media. *Nat. Commun.* **2017**, *8* (1), No. 14969.

(49) Haber, J.; Ungier, L. On Chemical Shifts of ESCA and Auger Lines in Cobalt Oxides. *J. Electron Spectrosc. Relat. Phenom.* **1977**, *12* (3), 305−312.

(50) Sarkar, B.; Das, D.; Nanda, K. K. Construction of Noble-Metal Alloys of Cobalt Confined N-Doped Carbon Polyhedra toward Efficient Water Splitting. *Green Chem.* **2020**, *22* (22), 7884−7895.

(51) Chong, L.; Wen, J.; Kubal, J.; Sen, F. G.; Zou, J.; Greeley, J.; Chan, M.; Barkholtz, H.; Ding, W.; Liu, D.-J. Ultralow-Loading Platinum-Cobalt Fuel Cell Catalysts Derived from Imidazolate Frameworks. *Science* **2018**, *362* (6420), 1276−1281.

(52) Liu, S.; Cao, W.; Wu, J.; Hu, E.; Zhang, J.; Gao, X.; Chen, Z. Integrated Pt_xCo_y-Hierarchical Carbon Matrix Electrocatalyst for Efficient Hydrogen Evolution Reaction. *ACS Appl. Mater. Interfaces* **2024**, *16* (1), 520−529.

(53) Hu, Y.; Guo, X.; Shen, T.; Zhu, Y.; Wang, D. Hollow Porous Carbon-Confined Atomically Ordered $PtCo_3$ Intermetallics for an Efficient Oxygen Reduction Reaction. *ACS Catal.* **2022**, *12* (9), 5380−5387.

(54) Han, S.; Li, H.; Li, T.; Chen, F.; Yang, R.; Yu, Y.; Zhang, B. Ultralow Overpotential Nitrate Reduction to Ammonia via a Three-Step Relay Mechanism. *Nat. Catal* **2023**, *6*, 402−414.

Supplementary Information

A Cobalt-Platinum-Ruthenium System for Acidic Methanol Oxidation

Hongbin Xu[1†], Daniel J. Zheng[1†], Haldrian Iriawan[1], Jen-Hung Fang[2], Junghwa Kim[1,2], Xiao Wang[3], Yuriy Román-Leshkov[3], Ju Li[1,4*], Yang Shao-Horn[1,2,5]*

Affiliations:
[1] Department of Materials Science and Engineering, Massachusetts Institute of Technology; Cambridge, MA 02139, USA
[2] Research Laboratory of Electronics, Massachusetts Institute of Technology; Cambridge, MA 02139, USA.
[3] Department of Chemical Engineering, Massachusetts Institute of Technology; Cambridge, MA 02139, USA
[4] Department of Nuclear Science and Engineering, Massachusetts Institute of Technology; Cambridge, MA 02139, USA
[5] Department of Mechanical Engineering, Massachusetts Institute of Technology; Cambridge, MA 02139, USA

*Correspondence: yroman@mit.edu (Yuriy Román-Leshkov); liju@mit.edu (Ju Li)

Supplementary Methods

Synthesis of Co-Pt/NC and Co-Ru/NC

The Co NP/NC was first prepared by pyrolysis of ZIF-67 at 1000 °C for 2 h under N_2 flow. 100 mg Co NPs/NC was dispersed in 50 mL H_2O and sonicated for 30 min. Then 5 mL H_2PtCl_6 hydrate (4 mg mL^{-1}) was added into above suspension and followed by stirring for 2 h to prepare the precursor of Co-Pt/NC. After centrifugation and drying overnight, the powder was heating to 900 °C with rate of 5 °C min^{-1} for 2 h under N_2 flow to obtain Co-Pt/NC. Similarly, the 5 mL $RuCl_3$ hydrate (4 mg mL^{-1}) was added and followed by same procedure to obtain Co-Ru/NC.

Synthesis of Pt-Ru/NC

To prepare the Pt-Ru/NC, other steps were kept same while ZIF-67 was changed to ZIF-8. ZIF-8 was prepared by the precipitation reaction between $Zn(NO_3)_2 \cdot 6H_2O$ (1.23 g) and 2-methylimidazole (1.46 g) in 50 mL methanol at ambient conditions. After 20 hours reaction, ZIF-8 was obtained by centrifugation and then washed with methanol three times, followed by drying in oven overnight. The pure NC was obtained by heating ZIF-8 to 1000 °C at rate of 5 °C min^{-1} for 2 h under N_2 flow. Zn was evaporated at that temperature due to its low boiling point. Pt-Ru/NC could be obtained by following the same steps as Co-Pt-Ru/NC.

Electrochemical measurements

The commercial PtRu/C was used to prepare ink for comparison. Typically, 5 mg PtRu/C was dispersed in a mixture with 9.99 mL of ethanol and 10 µL of Nafion (5 wt%) via ultrasonication for 60 min to form the catalyst ink. 10 µL of the prepared catalyst ink was dropped on the GC with a nominal loading of 20 μg_{PtRu} cm^{-2}_{geo}.

Specific electrochemical steps are as follows. First, electrochemical impedance spectroscopy was measured to confirm the whole setup and measure the solution resistance. Then the catalyst surface was cleaned by cyclic voltammetry (CV) in Ar-saturated 0.1 M $HClO_4$ solution at a scan rate of 200 mV s^{-1} with a potential range between ~0.05-1.2 V vs. RHE for around 100 cycles. The background current (without methanol) was collected in the same solution but with a scan rate of 50 mV s^{-1}. Then methanol was added to the 0.1 M $HClO_4$ supporting electrolyte to reach a concentration of 1 M. Then EIS was conducted again due to the change of electrolyte composition. After that, the CV and CA measurements were performed. The results are *iR* corrected and background corrected.

Determination of the electrochemical surface area (ESA)

The Pt ESA was obtained from integrating and averaging the net charge formation of hydrogen underpotential deposition in the range of 0.05 to 0.3 V in both forward and backward scan directions $[(Q_{UPD}(+) + Q_{UPD}(-))/2]$, which was then divided by 210 $\mu C/cm^2_{Pt}$ to obtain the ESA of Pt in catalysts.

DFT calculation

The different surface species of methanol electrooxidation ($*CH_2OH$, $*CH_2O$, $*CHOH$, $*CHO$, $*CO$, $*OH$, $*H_2O$) on the intermetallic structures were placed on one side of the slab. To convert the calculated DFT adsorption energies to Gibbs free energies, the zero point energies, enthalpic and entropic corrections from vibrational analysis have been taken from ref[1]). In modelling electrochemical reactions in Figure 5b, the gibbs free energy change of 0 eV has been defined to be gas-phase $CH_3OH(g)$ calculated as an ideal gas at 0.060 atm[1] (the vapor-liquid equilibrium value in water) and liquid H_2O (in equilibrium with water vapor pressure of 0.031 atm). The subsequent electrochemical steps were modelled as a sequential addition of $H^+ + e^-$ with the computational hydrogen electrode model[2], in which the free energy (G) of $H^+ + e^-$ is equal to $\frac{1}{2}H_2(g)$ at 1 bar. The placement of final state ($CO_2(g)$) relative to the initial state ($CH_3OH(g)$) on the energy scale has been done by using a thermodynamic approach, with $CO_2(g)$ at 1 atm, $CO_2(g)/CH_3OH(g)$ half cell potential of 0.02 V vs. RHE. Details of the DFT modeling and the thermodynamic approaches in this study follow those described in Ref2.

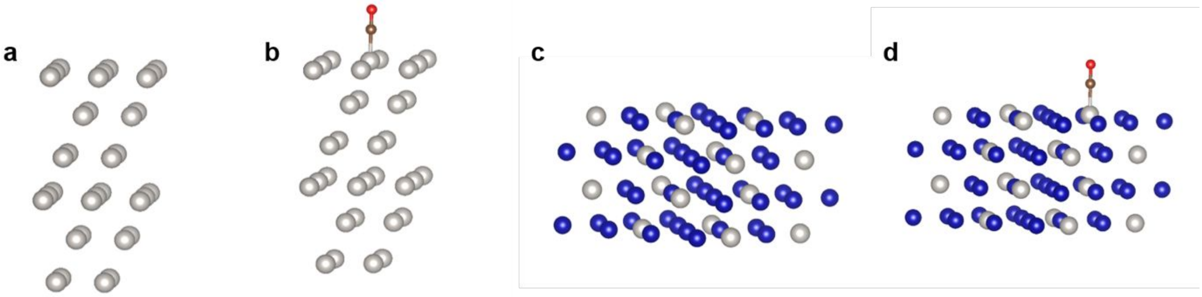

Figure S1. The DFT structure models for CO adsorption. (a) Slab of Pt (111) surface. (b) CO adsorption on Pt (111) surface. (c) Slab of Co_3Pt (100) surface. (d) CO adsorption on Pt site of Co_3Pt (100) surface.

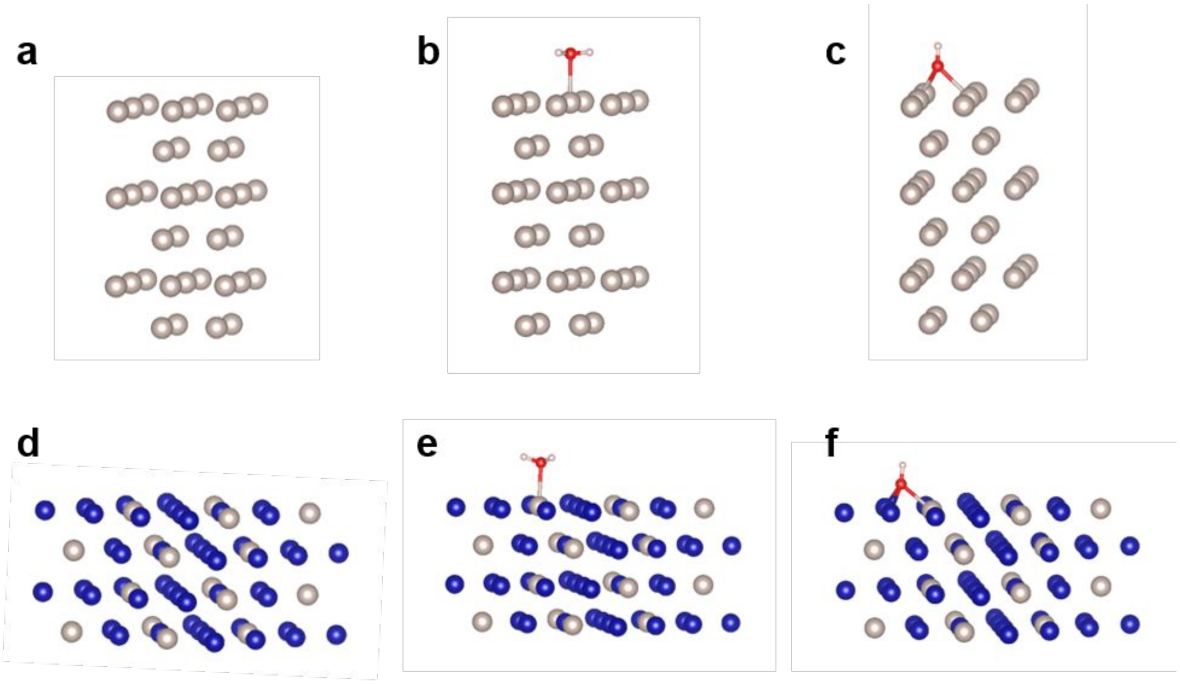

Figure S2. The DFT structure models for H_2O and OH adsorption. (a) Slab of Ru (0001) surface. H_2O (b) and OH (c) adsorption on Ru (0001) surface. (d) Slab of Co_3Ru (100) surface. H_2O (e) and OH (c) adsorption on Co_3Ru surface.

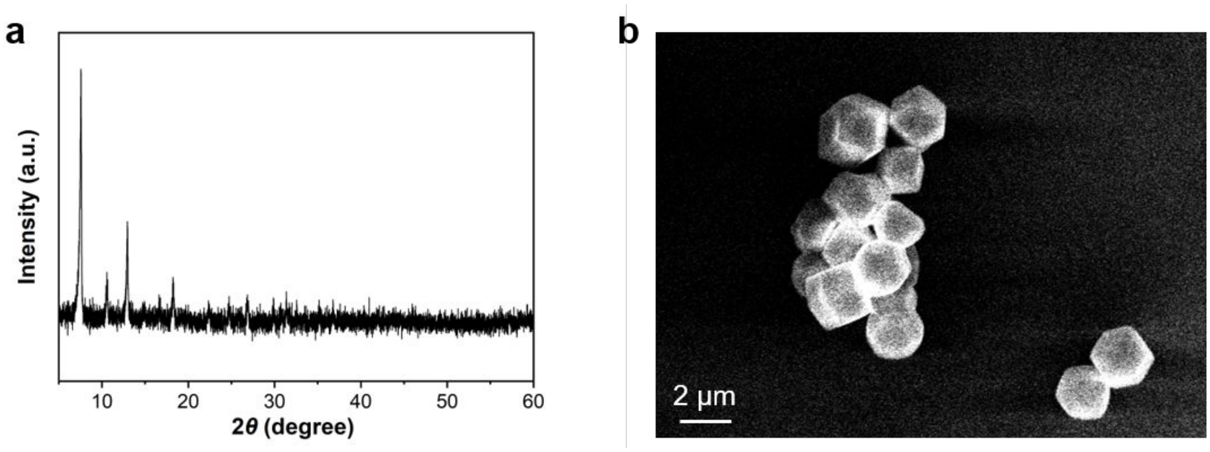

Figure S3. (a) XRD pattern of ZIF-67. (b) SEM image of ZIF-67.

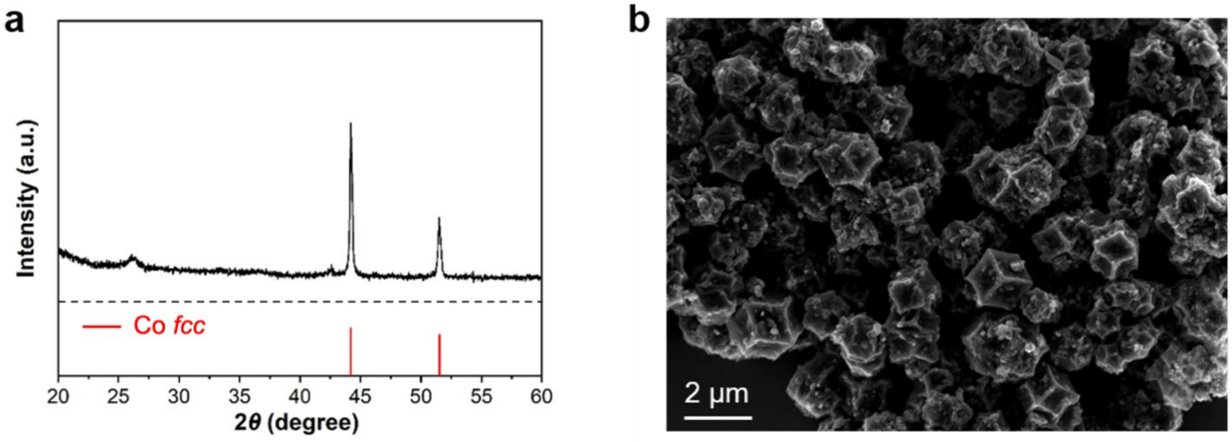

Figure S4. (a) XRD pattern of Co NPs/NC. (b) SEM image of Co NPs/NC. The Co NPs/NC maintained polyhedral morphology of ZIF-67 after pyrolysis.

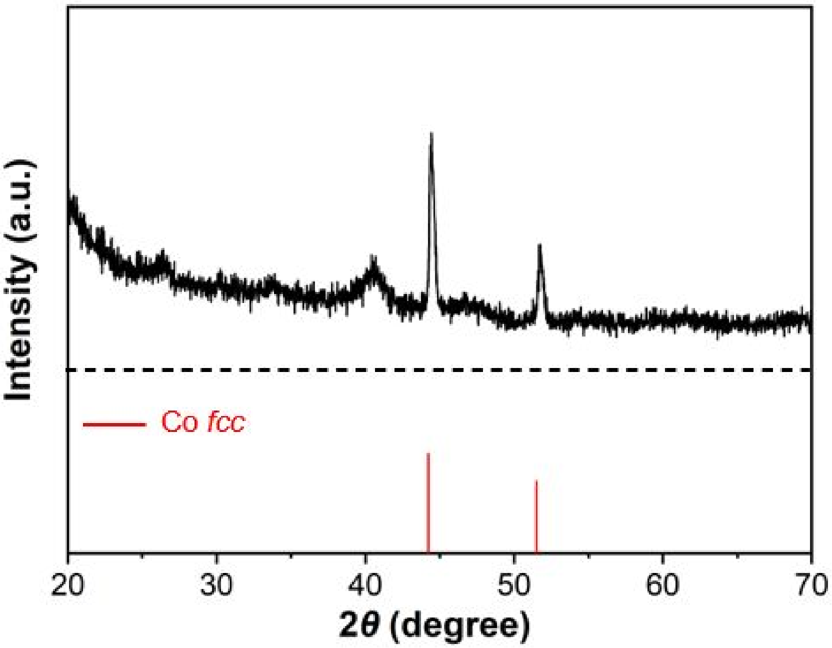

Figure S5. XRD pattern of Co+Pt+Ru/NC, the precursor after adsorption but before second pyrolysis.

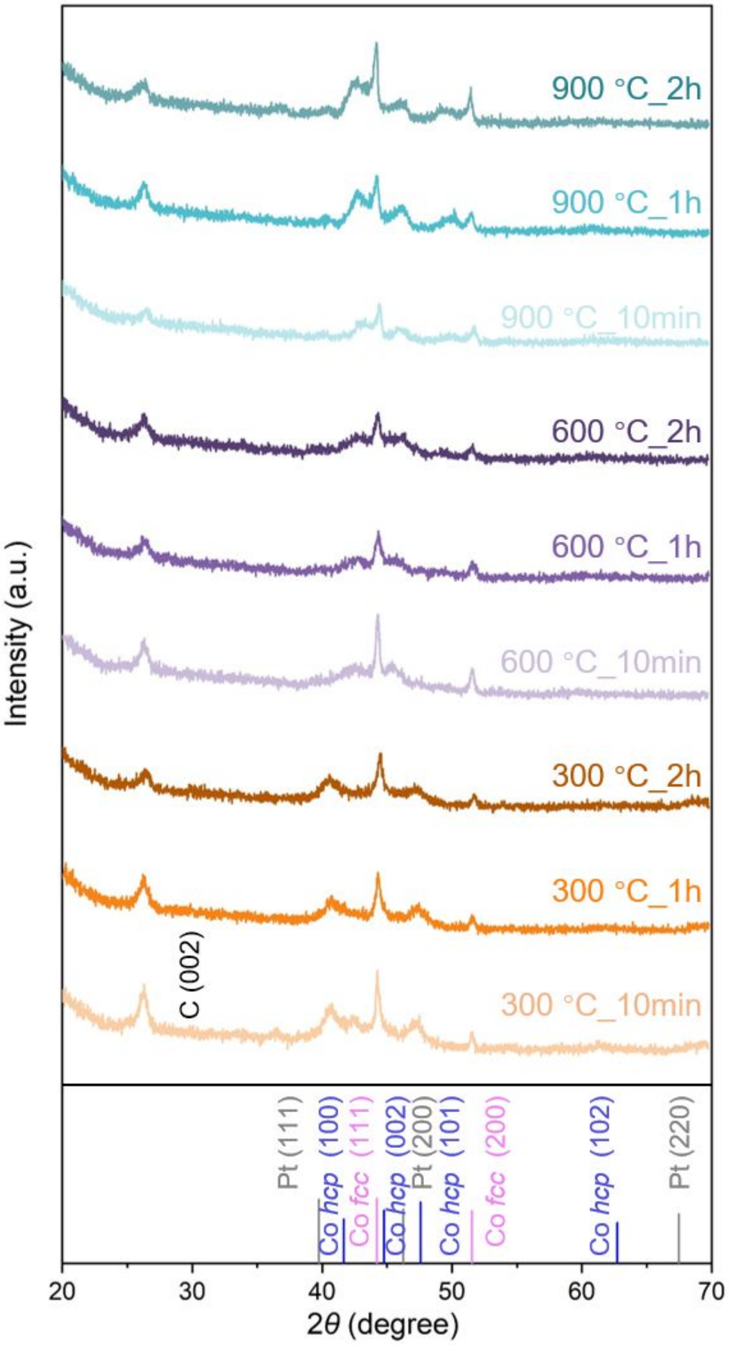

Figure S6. XRD patterns of catalysts synthesized at different conditions.

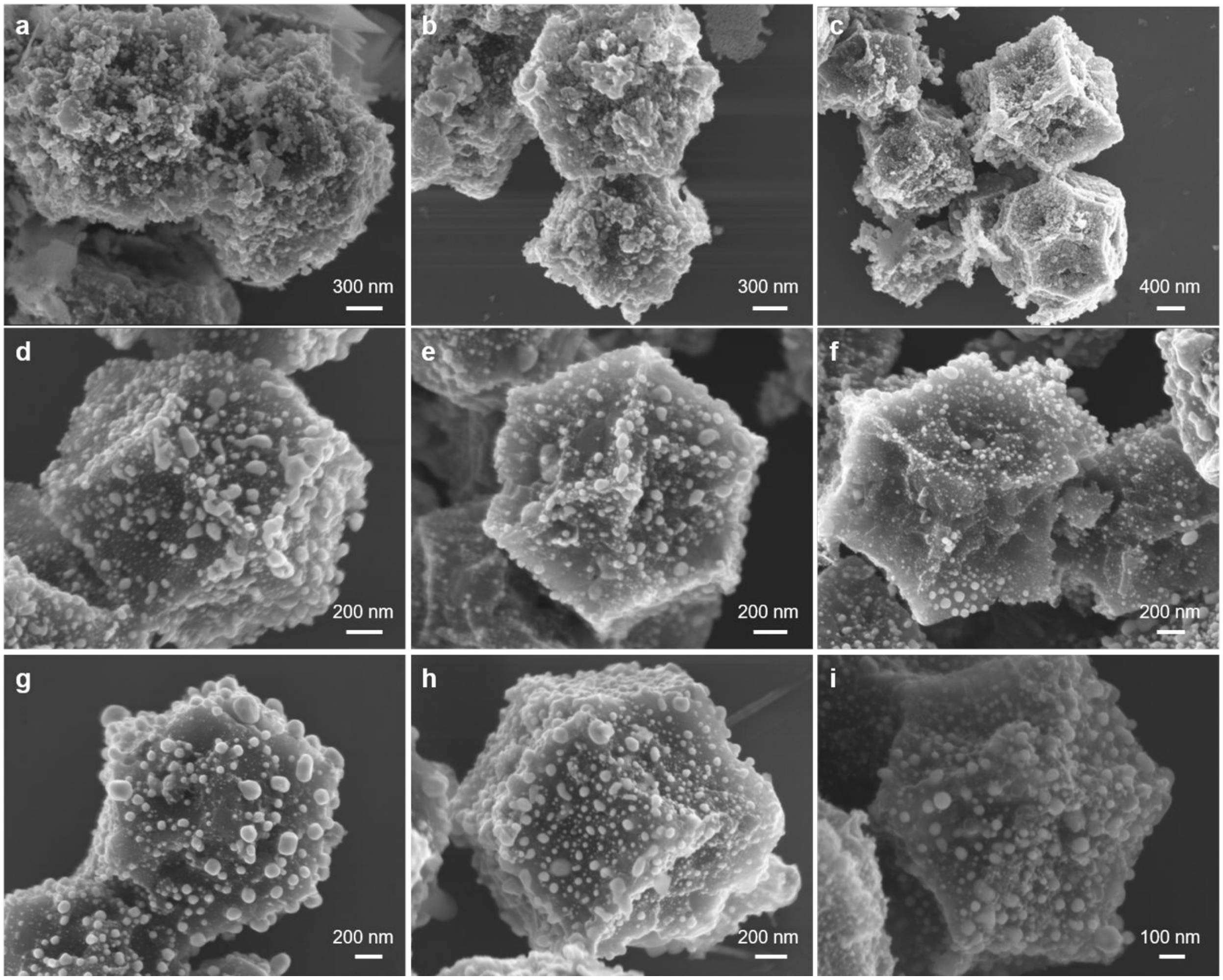

Figure S7. SEM image of samples synthesized at different conditions. (a) 300 °C_10 min; (b) 300 °C_1 h; (c) 300 °C_2 h; (d) 600 °C_10 min; (e) 600 °C_1 h; (f) 600 °C_2 h; (g) 900 °C_10 min; (h) 900 °C_1 h; (i) 900 °C_2 h.

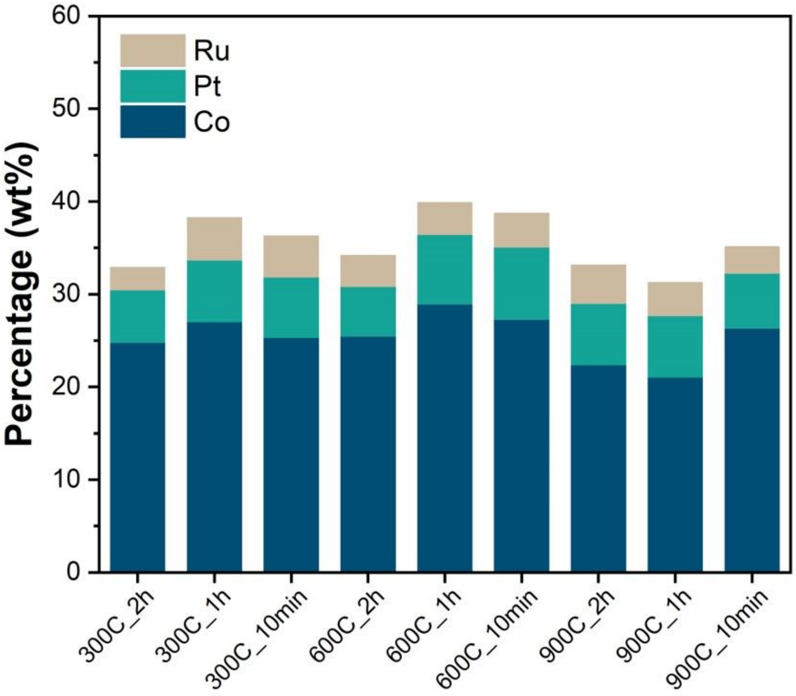

Figure S8. The metal weight percentage results of catalysts synthesized at different conditions by ICP-OES. The synthesis conditions are as follows: 300 °C for 10 min, 1h, 2h; 600 °C for 10 min, 1h, 2h; and 900 °C for 10 min, 1h, 2h.

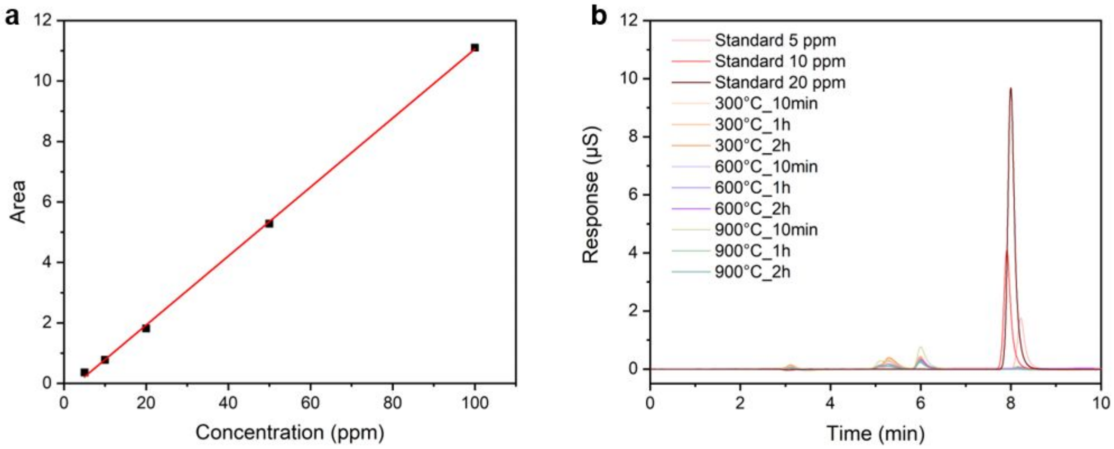

Figure S9. (a) Calibration curve of Cl^- by ion chromatography, $R^2 = 0.999$. (b) Cl^- measurements of different samples by ion chromatography. The peak of Cl^- is located around 8 min.

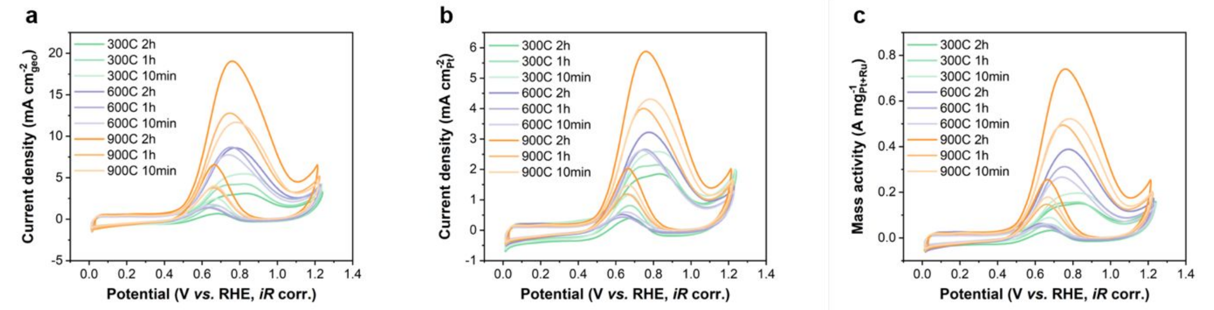

Figure S10. Cyclic voltammetry (CV) measurements for catalysts synthesized at different conditions. (a) geometrical activity. (b) Specific activity normalized by Pt electrochemical surface area. (c) Mass activity normalized by Pt+Ru.

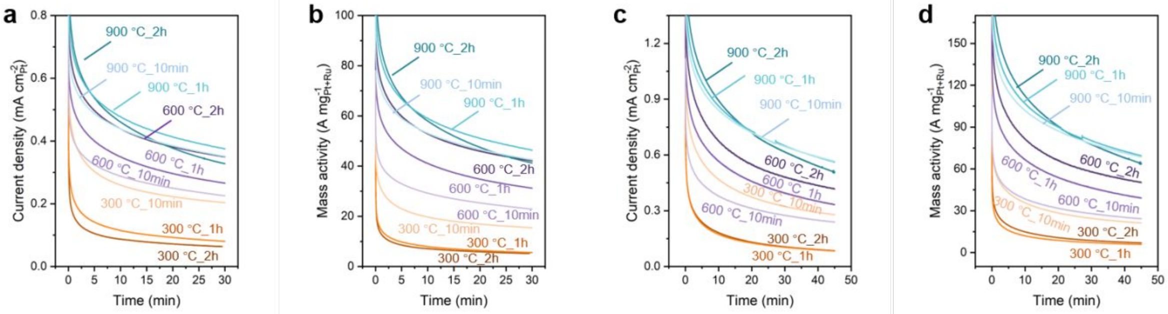

Figure S11. The specific and mass activity of chronoamperometry (CA) results at 0.6 (a, b) and 0.7 V_{RHE} (c, d) of Co-Pt-Ru/NC catalysts synthesized at different conditions.

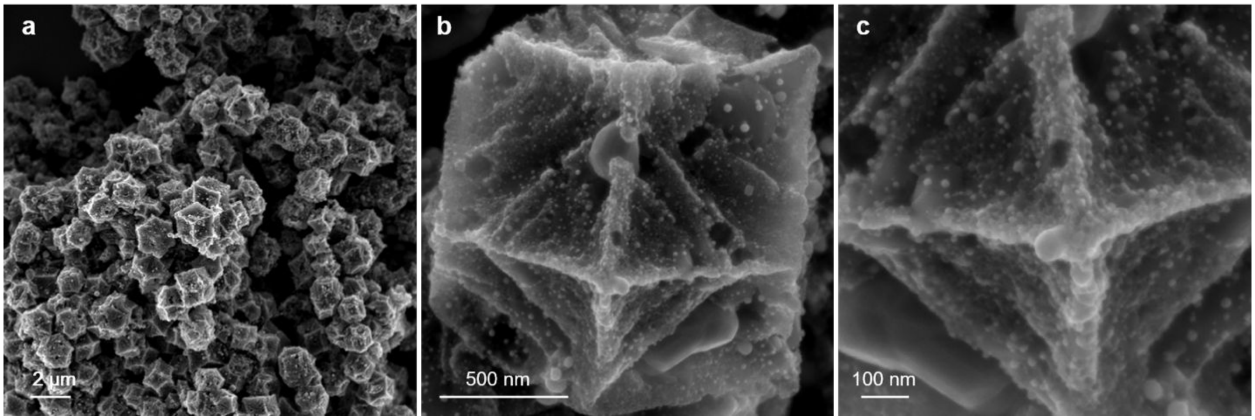

Figure S12. SEM images of Co-Pt-Ru/NC at different magnification. (a) Co-Pt-Ru/NC nanoparticles still maintained polyhedral morphology. A single dodecahedron (b) and local structure of one vertex (c) of Co-Pt-Ru/NC. The small nanoparticle on the dodecahedron is Co-Pt-Ru with carbon layer.

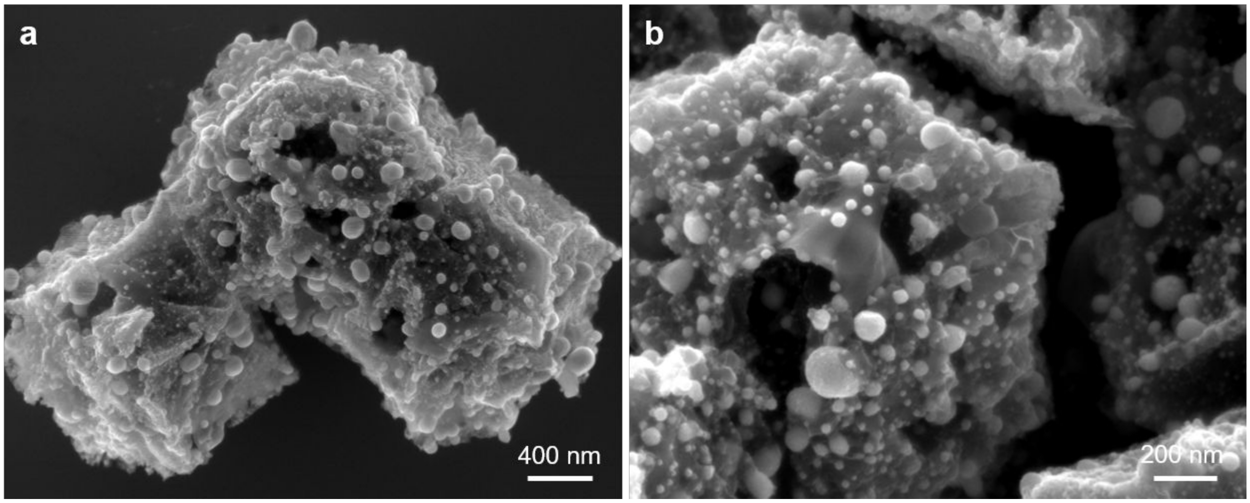

Figure S13. (a) The polyhedral structure of as-synthesized Co-Pt-Ru/NC. The hole on the polyhedron indicates the hollow structure of carbon skeleton. (b) A partial magnification to prove that this is a hollow structure.

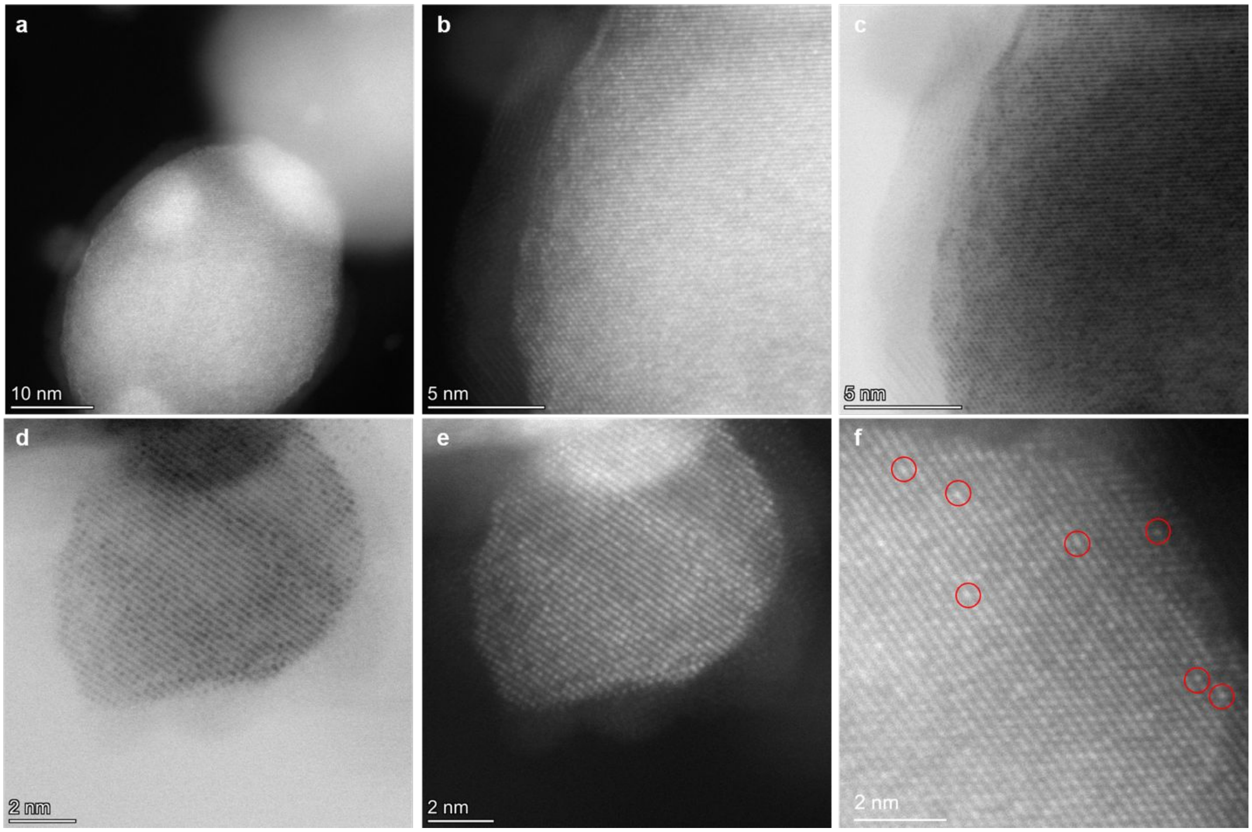

Figure S14. STEM images of $Co_{88}Pt_6Ru_6$/NC. HAADF-STEM images (a and b), bright field STEM image (c) of $Co_{88}Pt_6Ru_6$/NC. There is a carbon layer on the outside of nanoparticle. Bright field (d) and dark field (e) of a $Co_{88}Pt_6Ru_6$ nanoparticle to cross-verified different atoms. The darker atoms in (c) and (d) confirm the existence of Pt and Ru. The brighter atoms in (b), (e), and circled in (f) are Pt atoms or Ru atoms on Co support due to the higher atomic number of Pt and Ru compared to Co.

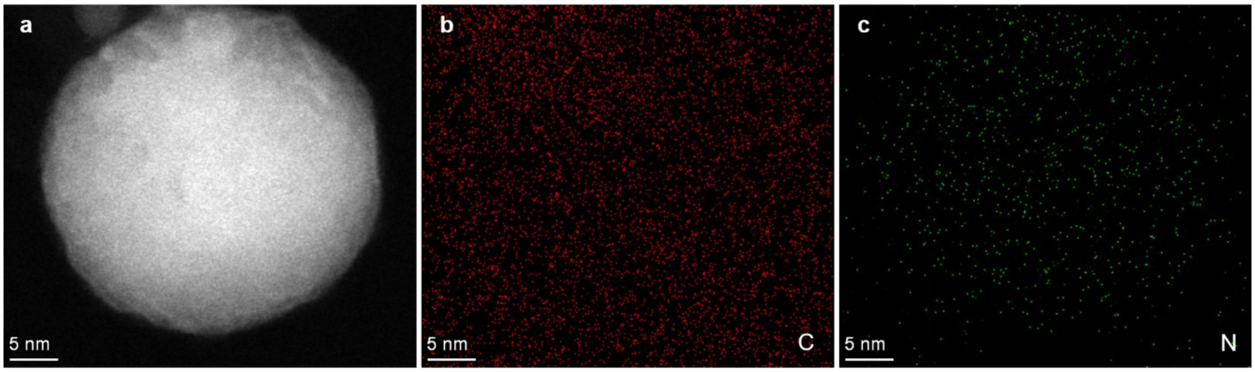

Figure S15. HAADF-STEM image (a) of $Co_{88}Pt_6Ru_6$/NC and corresponding EDX mapping of C (b) and (c).

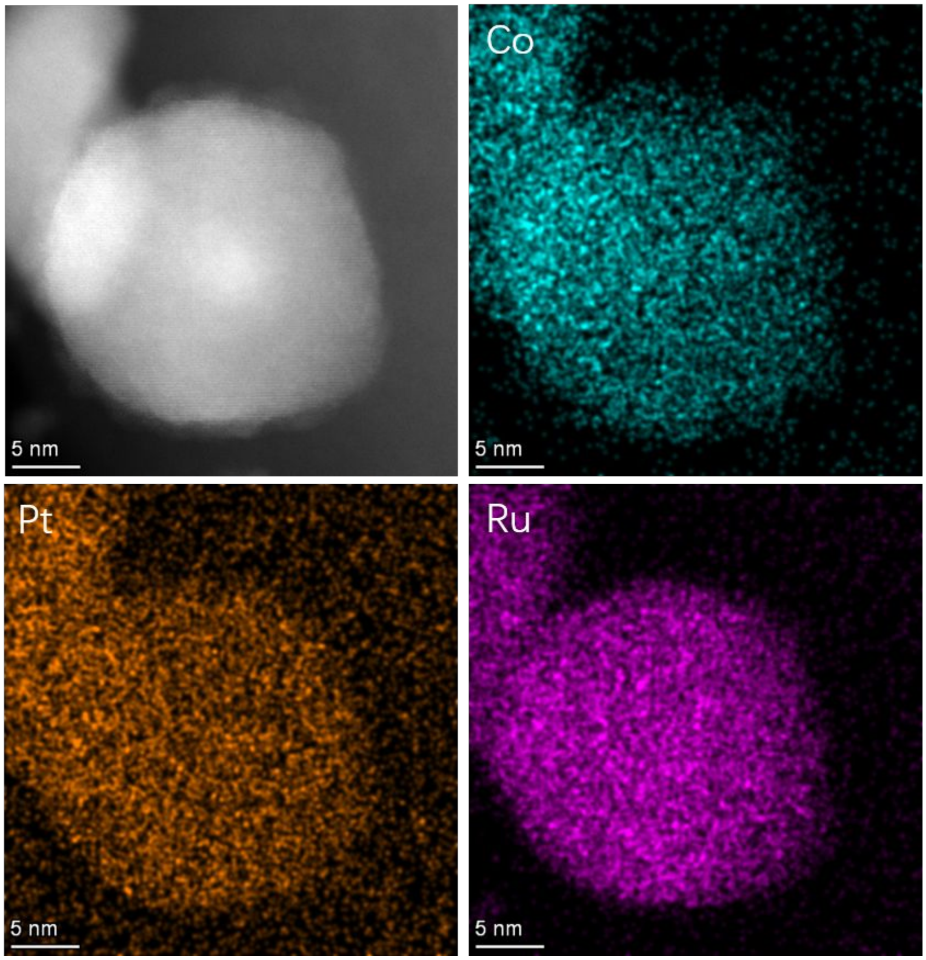

Figure S16. HAADF-STEM image and corresponding elements EDX mapping of $Co_{88}Pt_6Ru_6$/NC. The normalized atomic metal composition is, Co: 67.4%, Pt: 15.2%, and Ru: 17.4%.

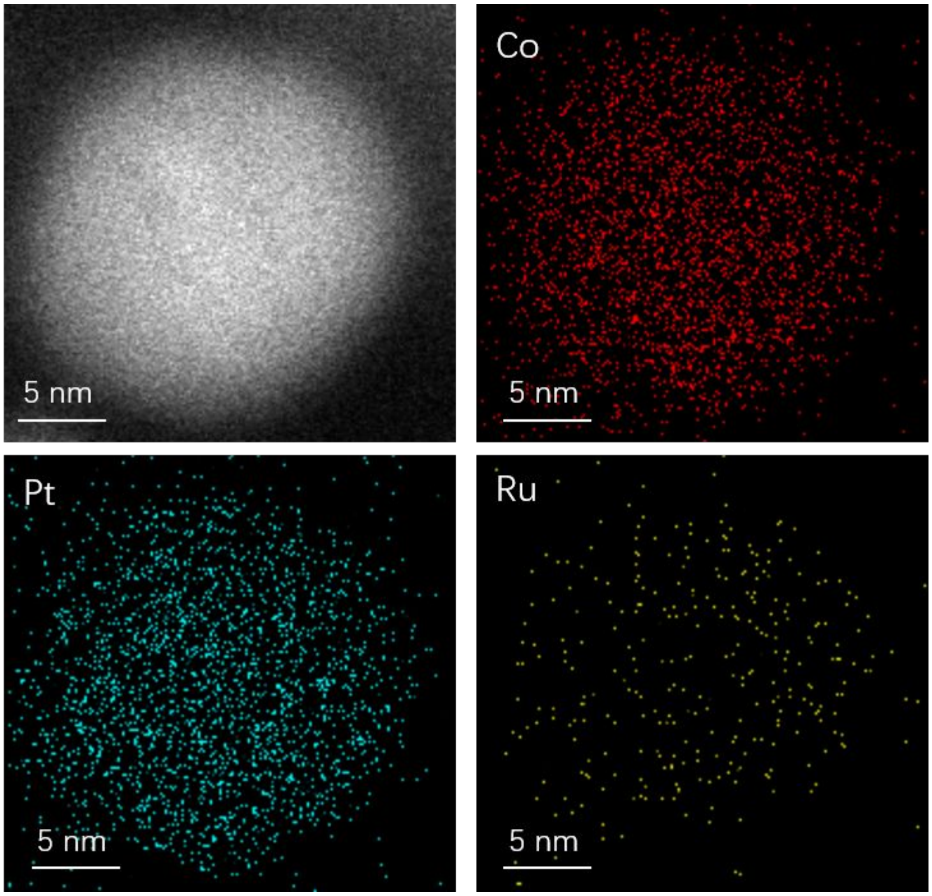

Figure S17. HAADF-STEM image and corresponding elements EDX mapping of $Co_{88}Pt_6Ru_6$/NC. The normalized atomic metal composition is, Co: 63.8%, Pt: 18.1%, and Ru: 18.1%.

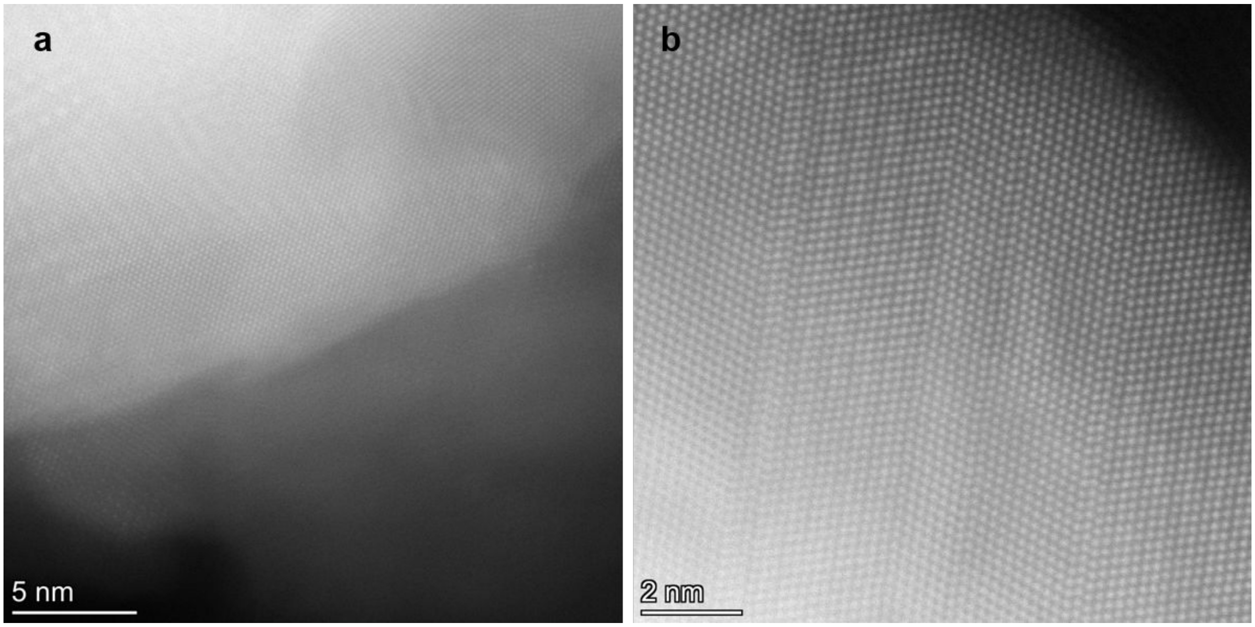

Figure S18. High-angle annular dark field scanning transmission electron microscopy (HAADF-STEM) images (a and b) of Co NPs/NC.

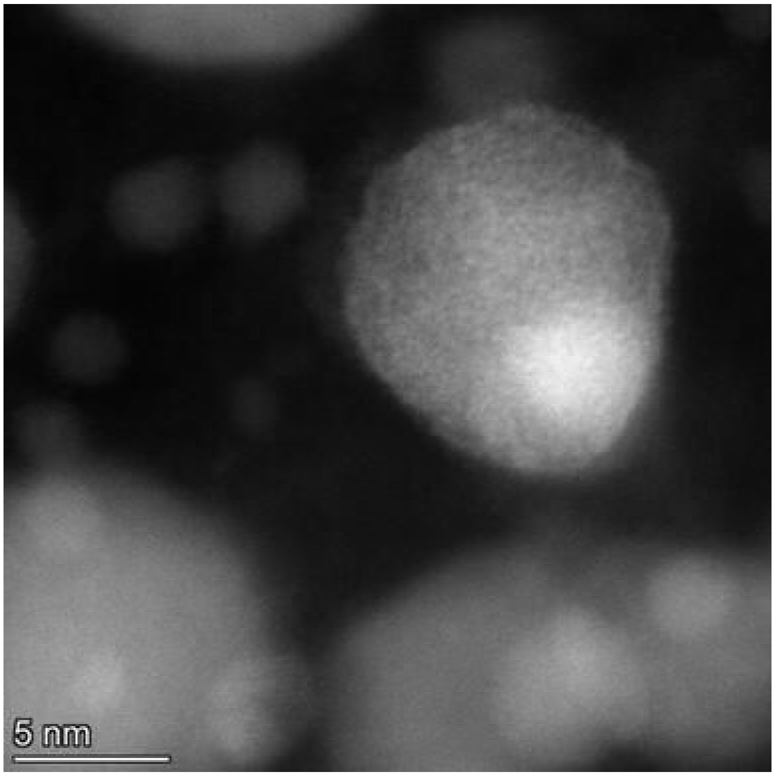

Figure S19. HAADF-STEM images of $Co_{88}Pt_6Ru_6$/NC. In some nanoparticles, the lattice fringes cannot be observed clearly due to the Pt and Ru doping.

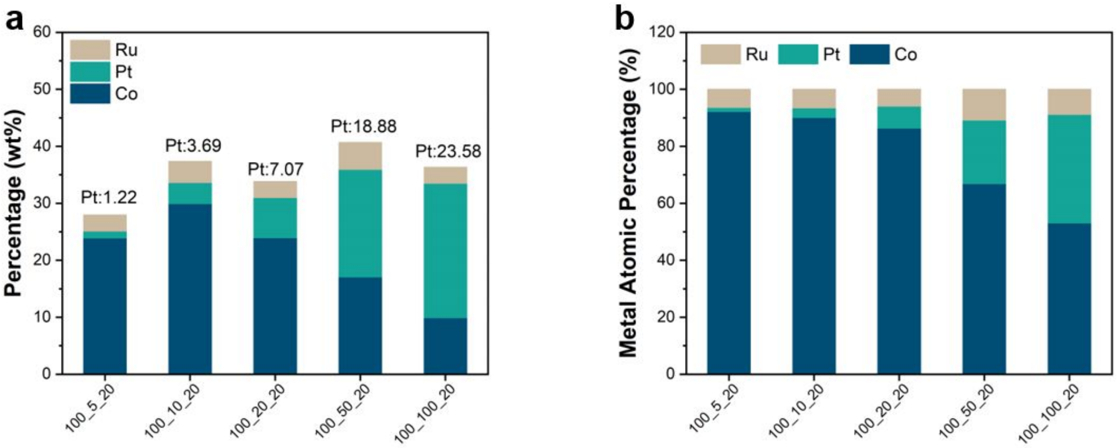

Figure S20. ICP-OES results of different Pt loading catalysts. Metal weight percentage (a) and metal atomic percentage (b) of different Pt loading catalysts. The number on the X-axis represents the amount of different precursors at the time of synthesis.

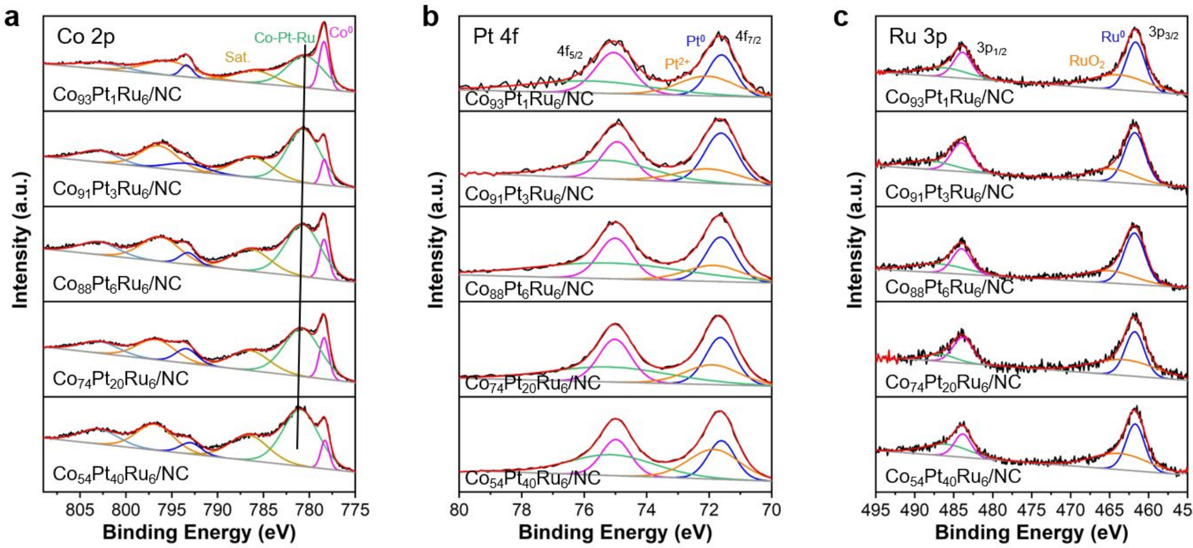

Figure S21. X-ray photoelectron spectroscopy (XPS) spectra of different Pt loading catalyst. (a) Co 2p. (b) Pt 4f. (c) Ru 3p.

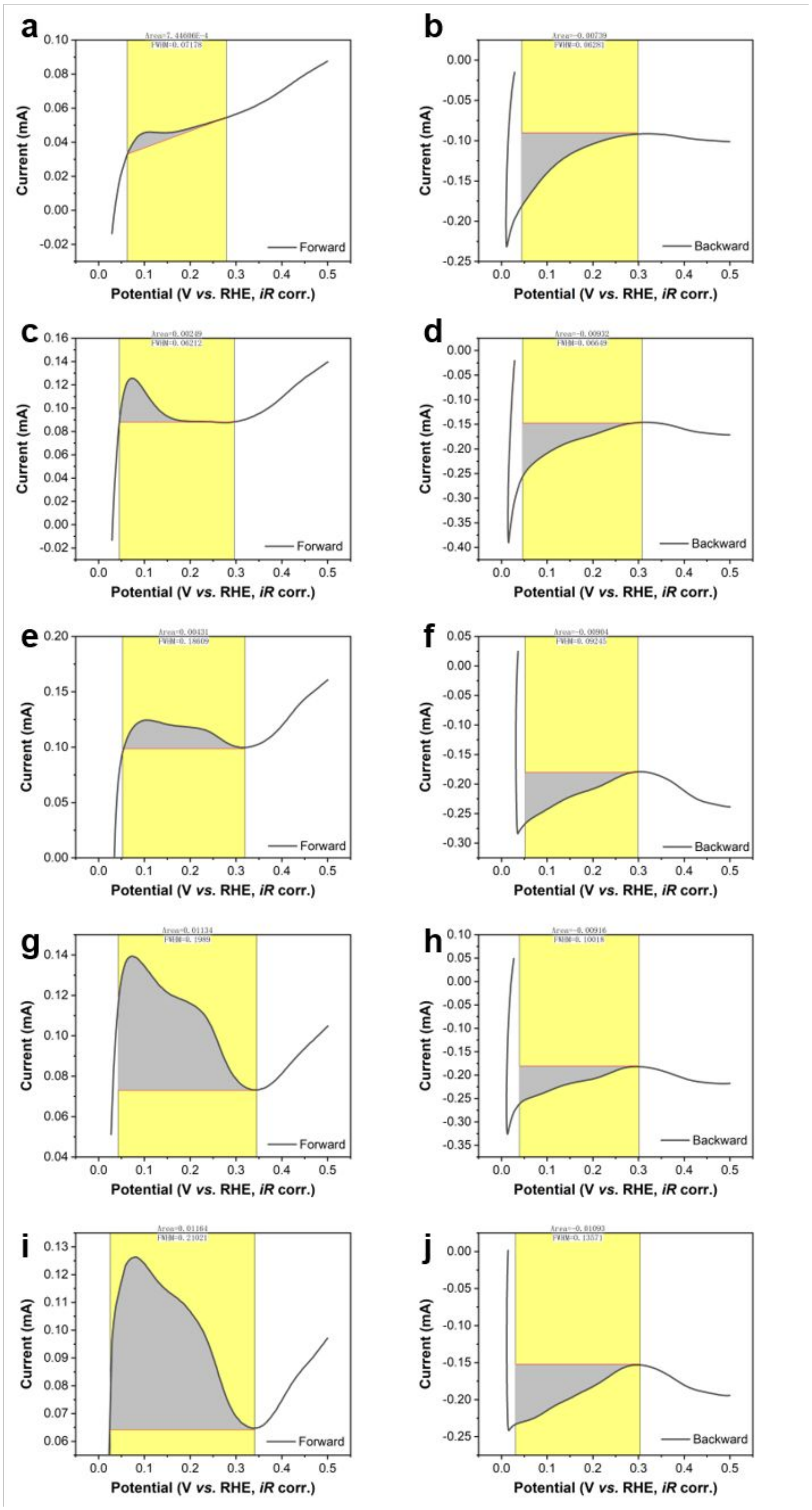

Figure S22. Hydrogen underpotential deposition (HUPD) integration for forward and backward scan of (a, b) $Co_{93}Pt_1Ru_6$/NC, (c, d) $Co_{91}Pt_3Ru_6$/NC, (e, f) $Co_{88}Pt_6Ru_6$/NC, (g, h) $Co_{74}Pt_{20}Ru_6$/NC, and (i, j) $Co_{54}Pt_{40}Ru_6$/NC.

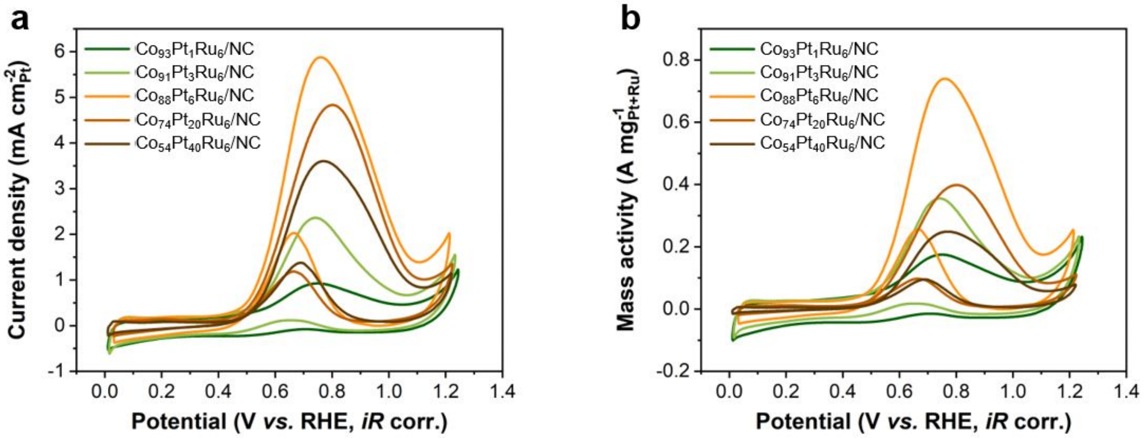

Figure S23. CV of different Pt loading catalysts. (a) Specific activity. (b) Mass activity. The CV was measured in Ar-saturated 0.1 M $HClO_4$ solution with 1 M CH_3OH at a scan rate of 50 mV s^{-1}.

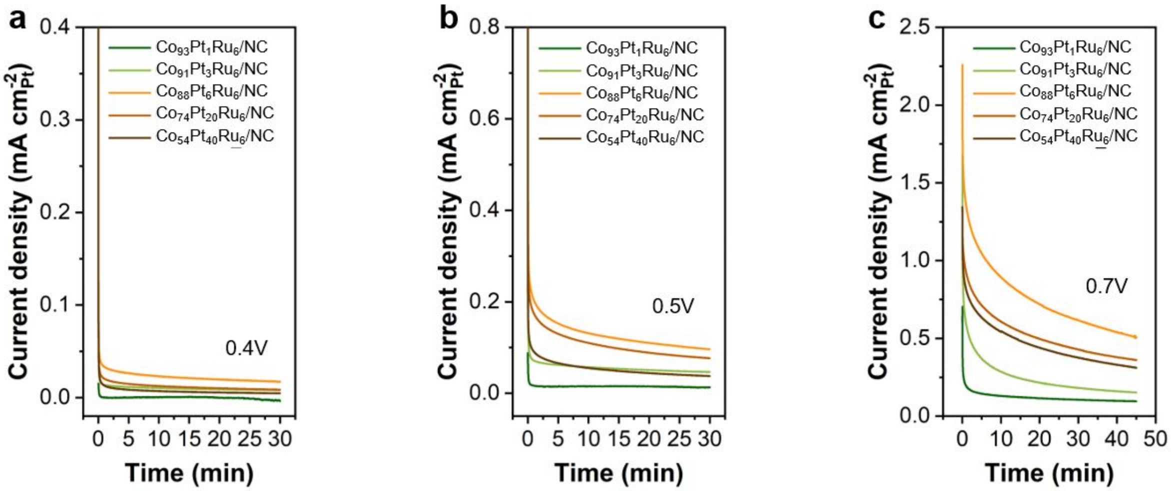

Figure S24. Specific activity of CA measurements for different Pt loading catalysts. The applied potential is 0.4 V (a), 0.5 V (b), 0.7 V (c) vs. RHE.

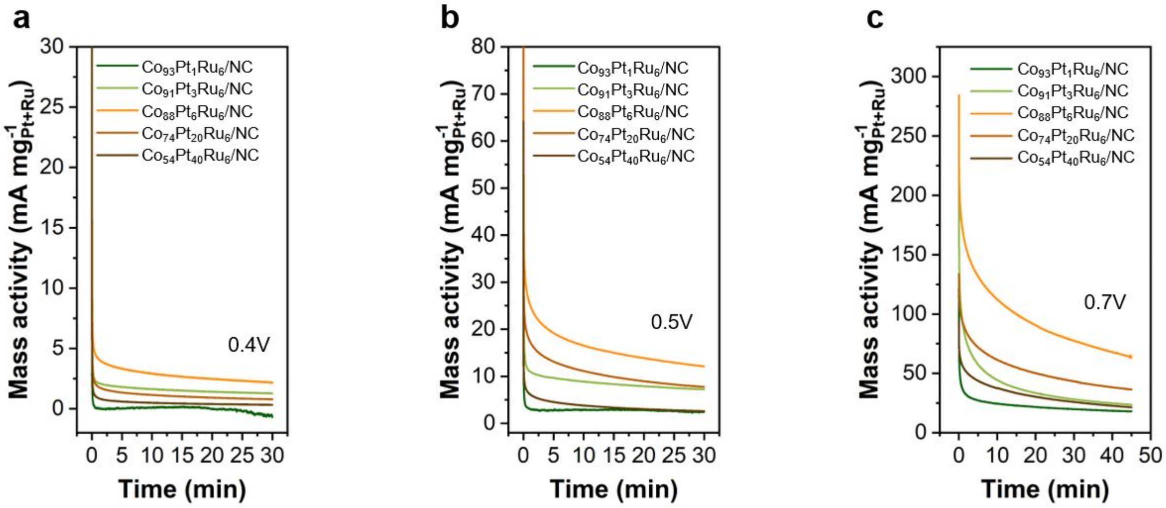

Figure S25. Mass activity of CA measurements for different Pt loading catalysts. The applied potential is 0.4 V (a), 0.5 V (b), 0.7 V (c) vs. RHE.

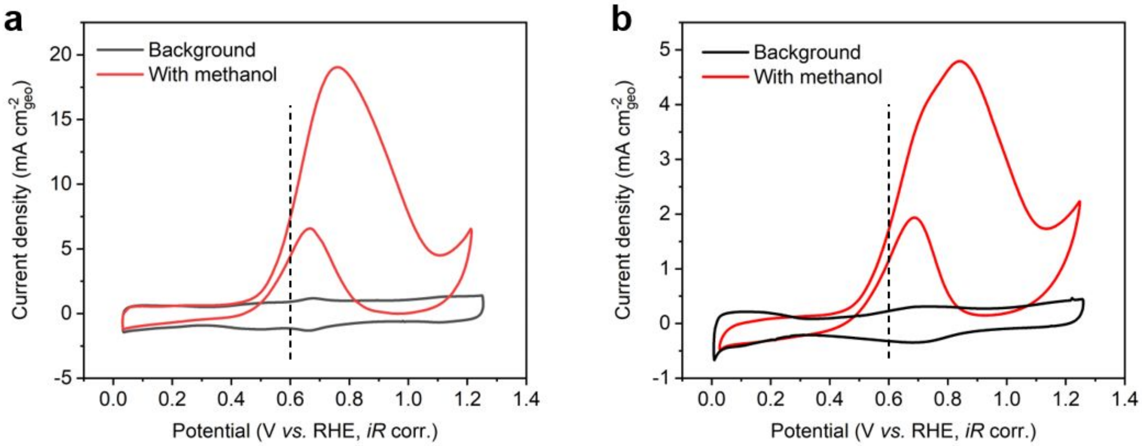

Figure S26. CV for geometric activity of (a) $Co_{88}Pt_6Ru_6$/NC and (b) commercial PtRu/C with background. To do background correction, The corrected current is obtained by subtracting the background current at the same potential. The CV with methanol was measured in Ar-saturated 0.1 M $HClO_4$ solution with 1 M CH_3OH at a scan rate of 50 mV s^{-1}. The CV of background was measured in Ar-saturated 0.1 M $HClO_4$ solution at a scan rate of 50 mV s^{-1}.

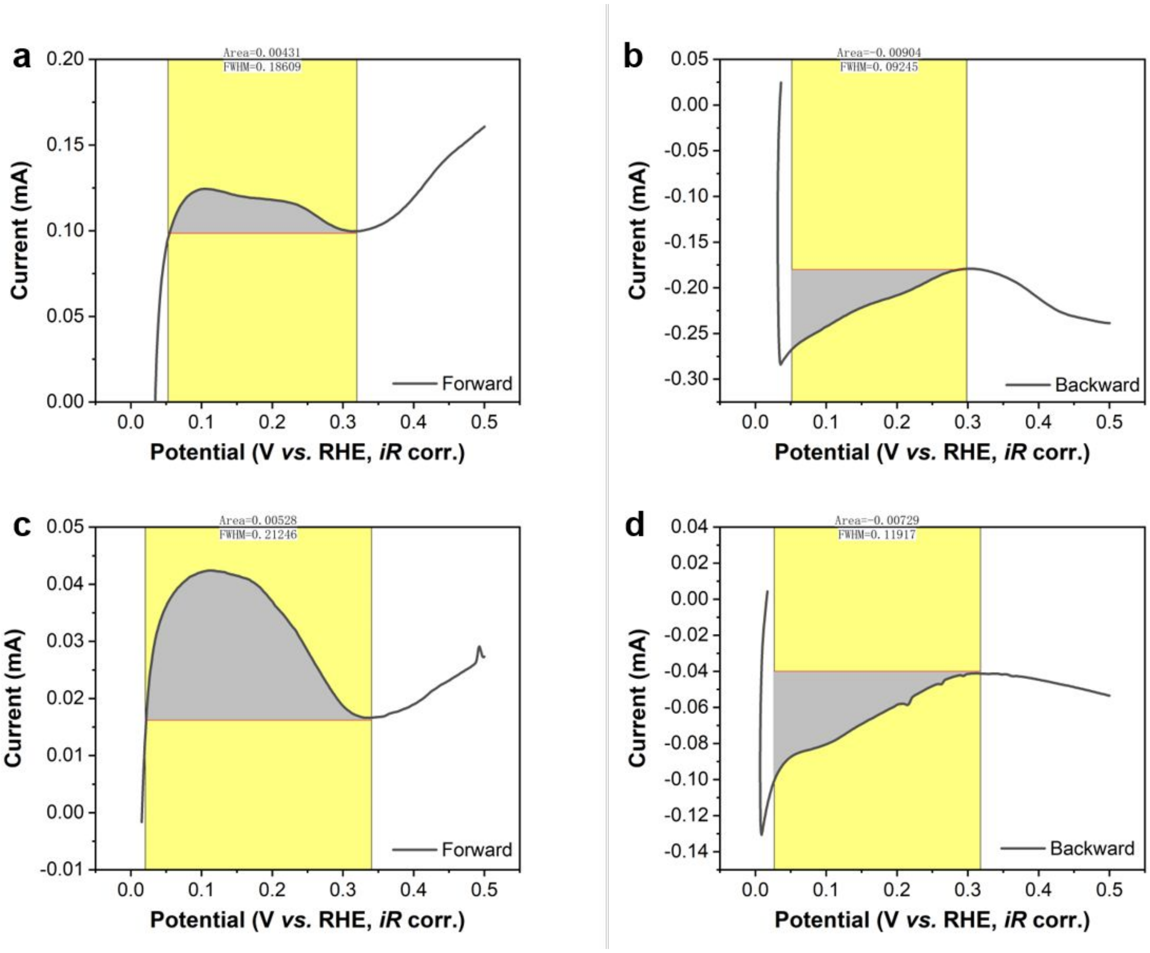

Figure S27. Hydrogen underpotential deposition (HUPD) integration for forward and backward scan of (a, b) $Co_{88}Pt_6Ru_6$/NC and (c, d) commercial PtRu/C.

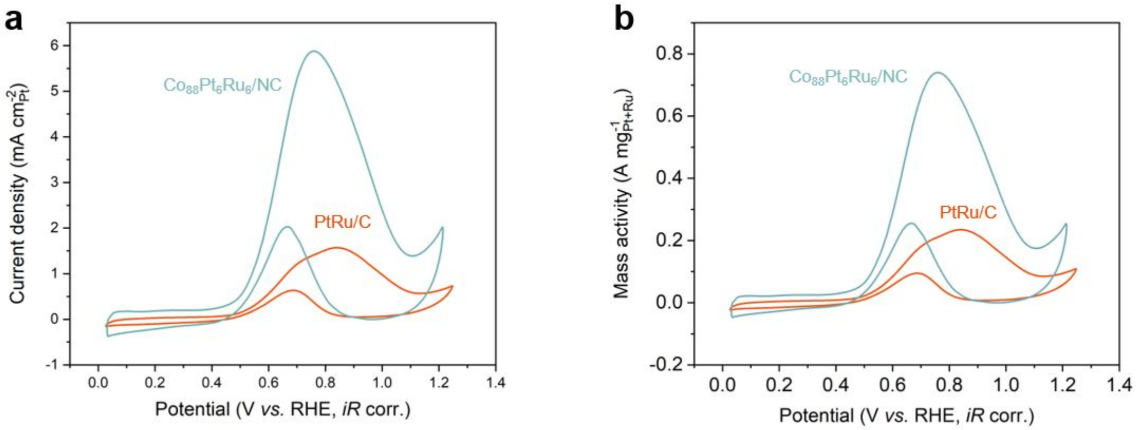

Figure S28. CV of optimized Co$_{88}$Pt$_6$Ru$_6$/NC and commercial PtRu/NC. (a) Specific activity. (b) Mass activity. The CV was measured in Ar-saturated 0.1 M HClO$_4$ solution with 1 M CH$_3$OH at a scan rate of 50 mV s^{-1}.

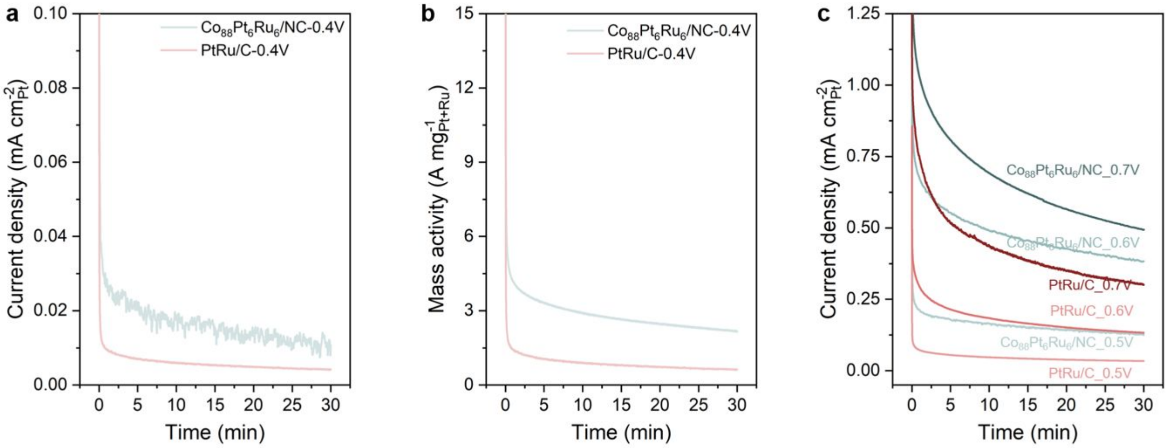

Figure S29. CA measurements of optimized $Co_{88}Pt_6Ru_6$/NC compared with a commercial PtRu/C catalyst. Specific (a) and mass activity (b) of at 0.4V vs. RHE. Specific activity (c) of CA at 0.5-0.7 V vs. RHE.

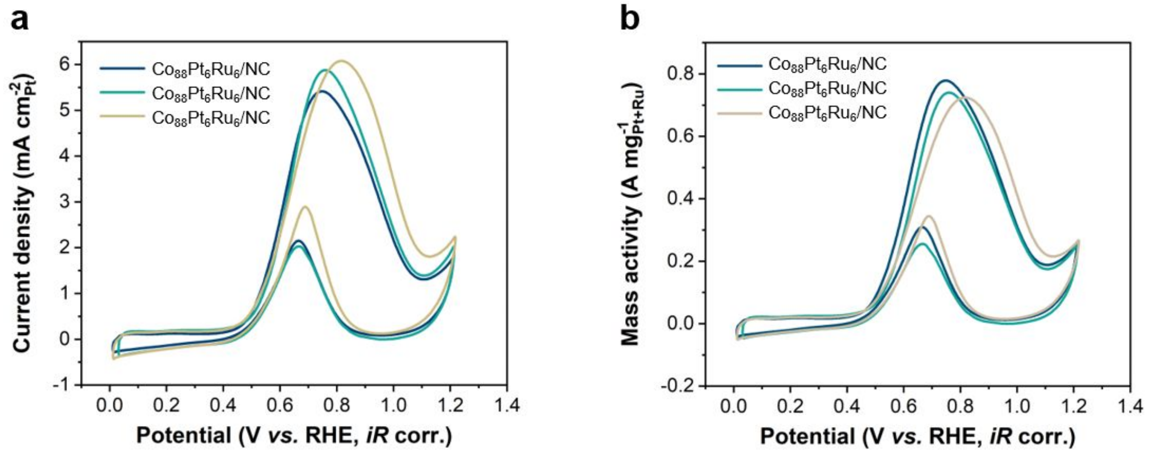

Figure S30. Repeated CV measurements of optimized Co$_{88}$Pt$_6$Ru$_6$/NC. (a) Specific activity. (b) Mass activity. The CV was measured in Ar-saturated 0.1 M HClO$_4$ solution with 1 M CH$_3$OH at a scan rate of 50 mV s^{-1}.

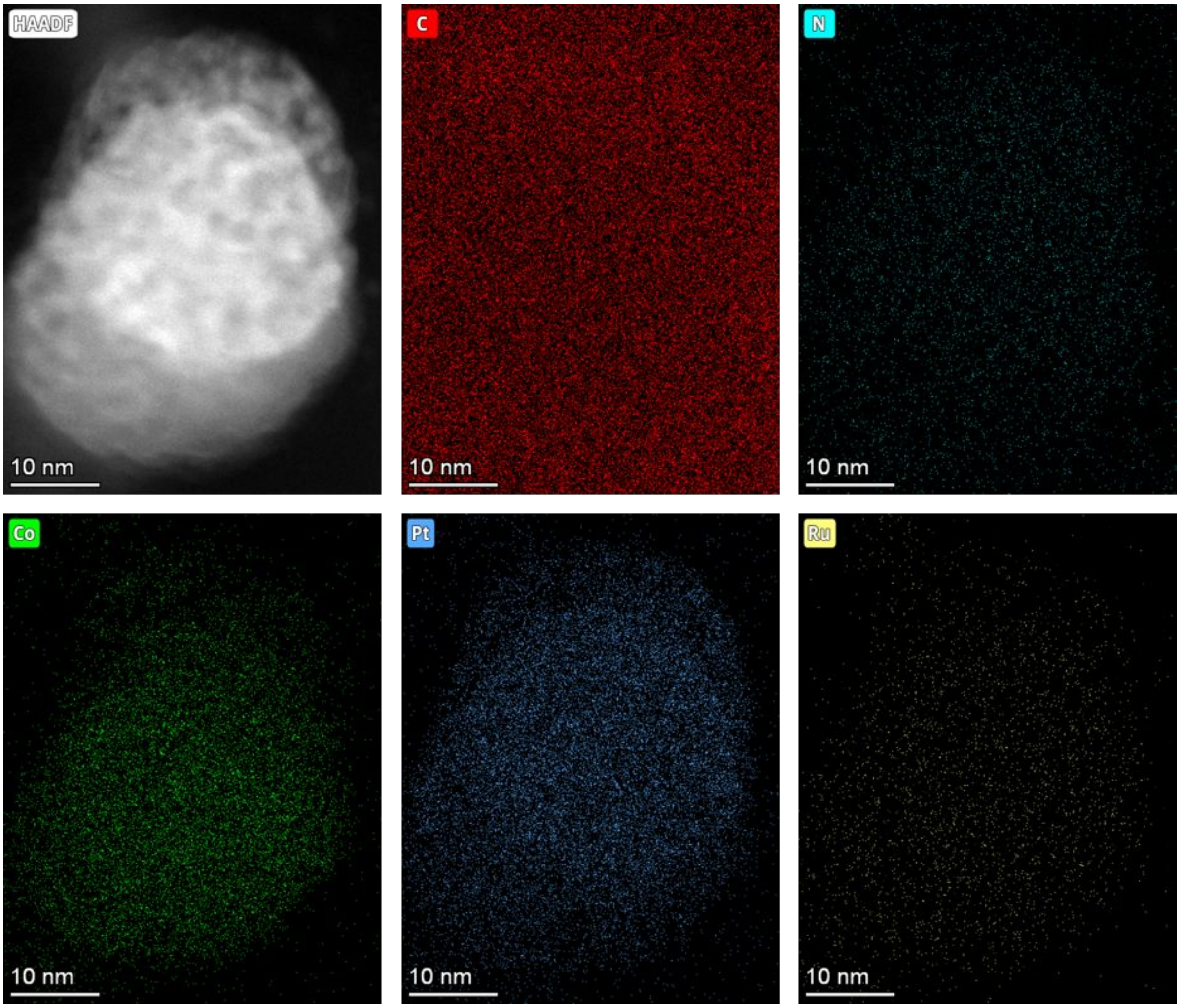

Figure S31. HAADF-STEM image and corresponding EDX element mapping of $Co_{88}Pt_6Ru_6$/NC after MOR measurements. The normalized atomic metal composition is, Co: 39.2%, Pt: 30.9%, and Ru: 29.9%.

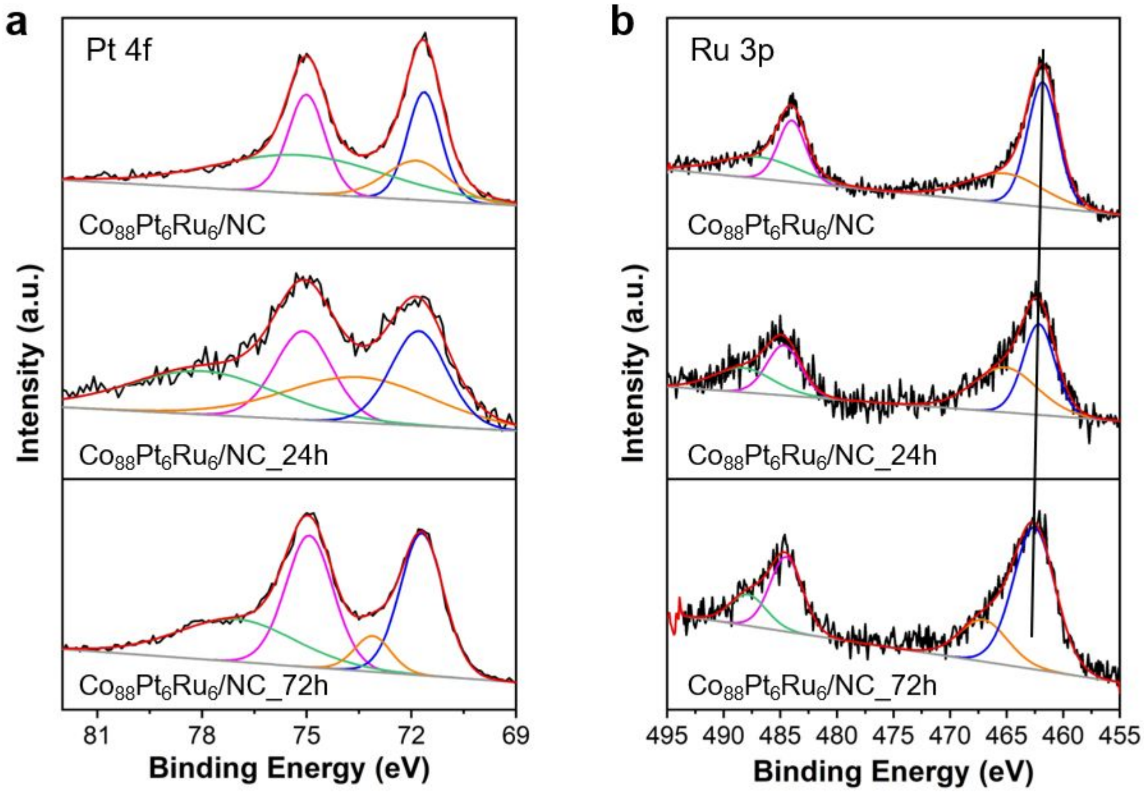

Figure S32. XPS spectra of Co$_{88}$Pt$_6$Ru$_6$/NC after acid treatment. (a) Pt 4f. (b) Ru 3p.

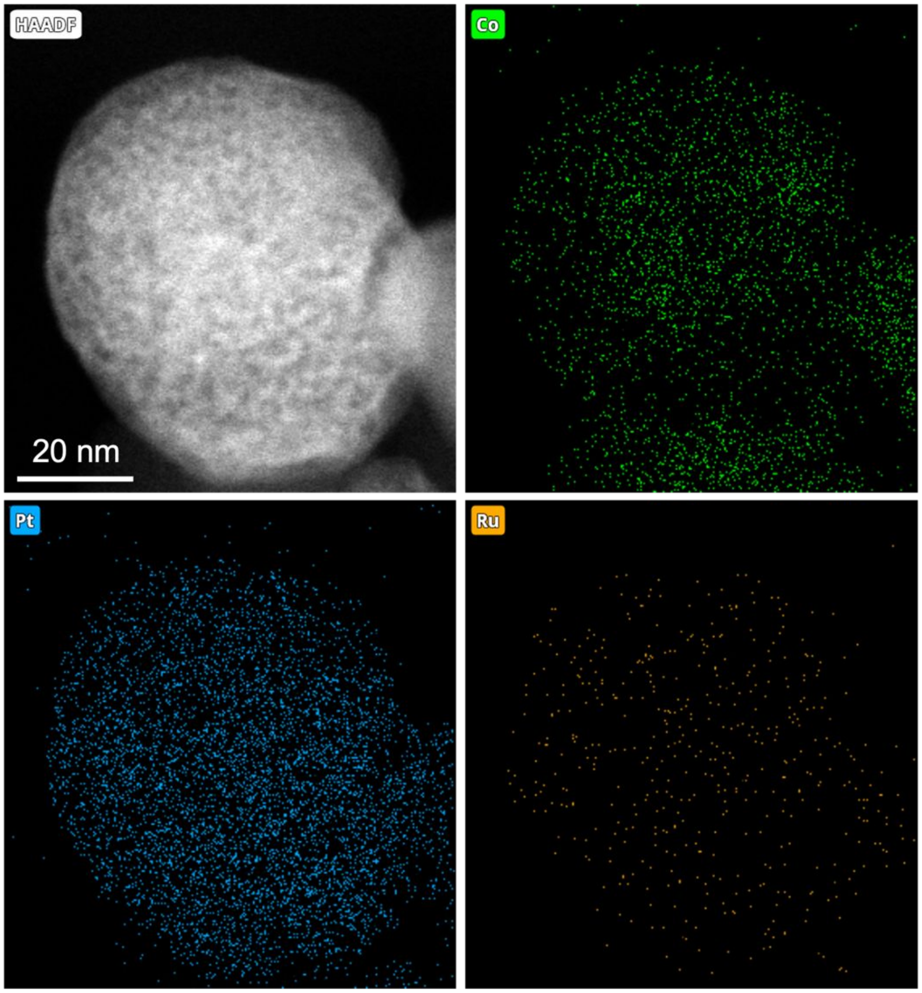

Figure S33. HAADF-STEM image and corresponding EDX element mapping of $Co_{88}Pt_6Ru_6$/NC after 24h acid treatment. The normalized atomic metal composition is, Co: 37.2%, Pt: 32.7%, and Ru: 30.1%.

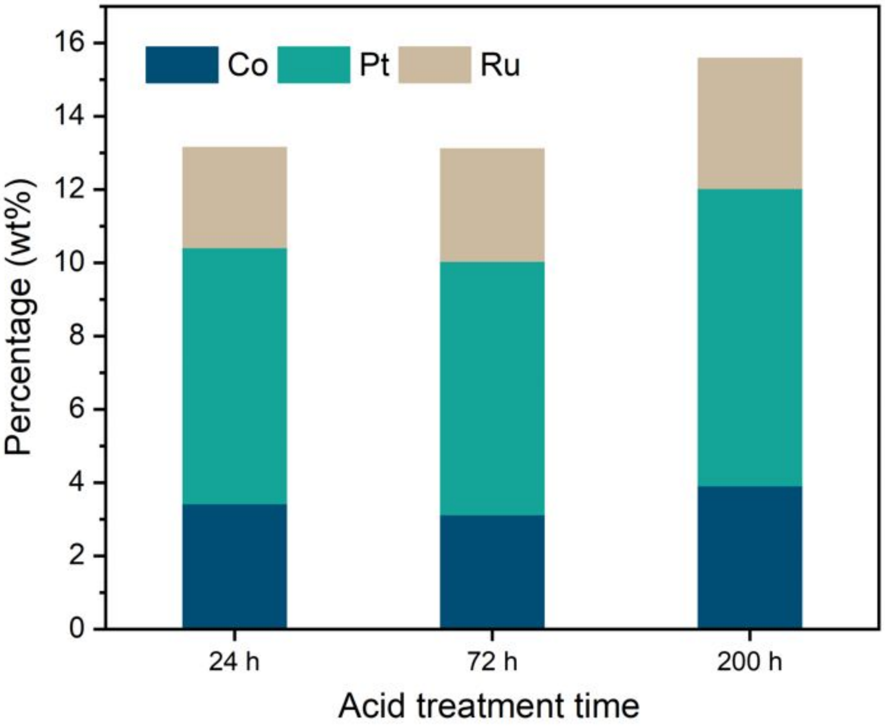

Figure S34. The metal weight percentage results by ICP-OES of $Co_{88}Pt_6Ru_6$/NC after acid treatment.

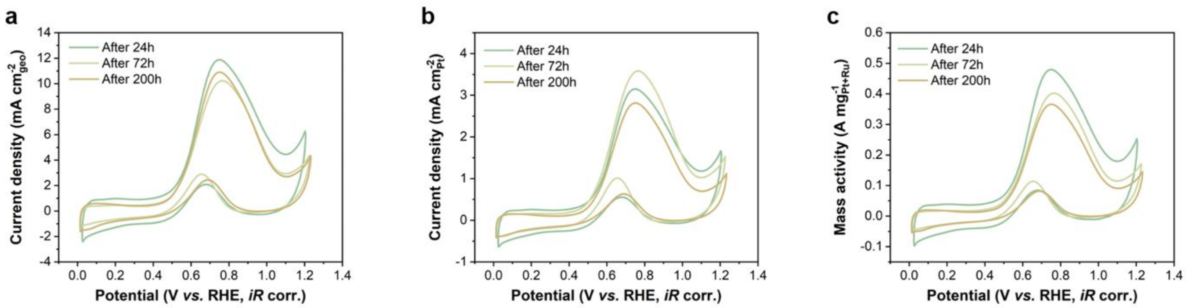

Figure S35. CV of $Co_{88}Pt_6Ru_6$/NC after acid treatment for different time. (a) Geometrical activity. (b) Specific activity. (c) Mass activity. The CV was measured in Ar-saturated 0.1 M $HClO_4$ solution with 1 M CH_3OH at a scan rate of 50 mV s^{-1}.

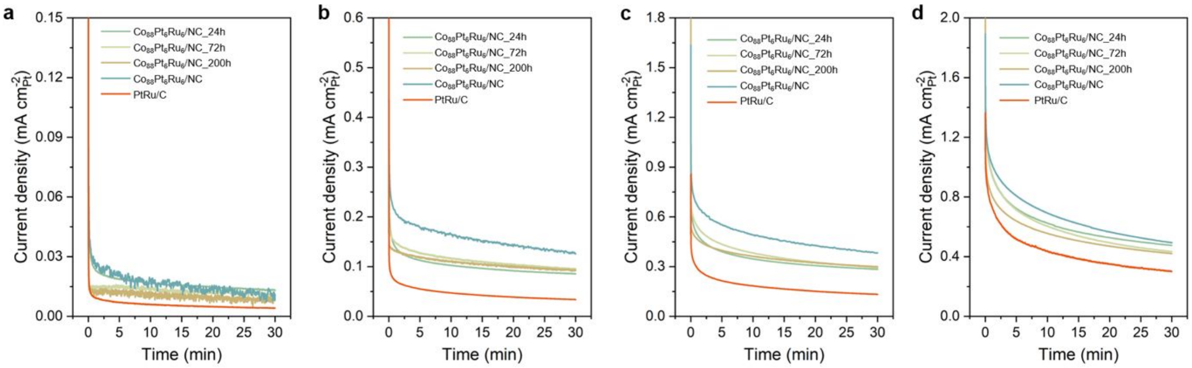

Figure S36. Specific activity of CA measurements for $Co_{88}Pt_6Ru_6$/NC after acid treatment and compared with $Co_{88}Pt_6Ru_6$/NC before acid treatment and commercial PtRu/C. The applied potential is 0.4 V (a), 0.5 V (b), 0.6 V (c), and 0.7 V (d) vs. RHE.

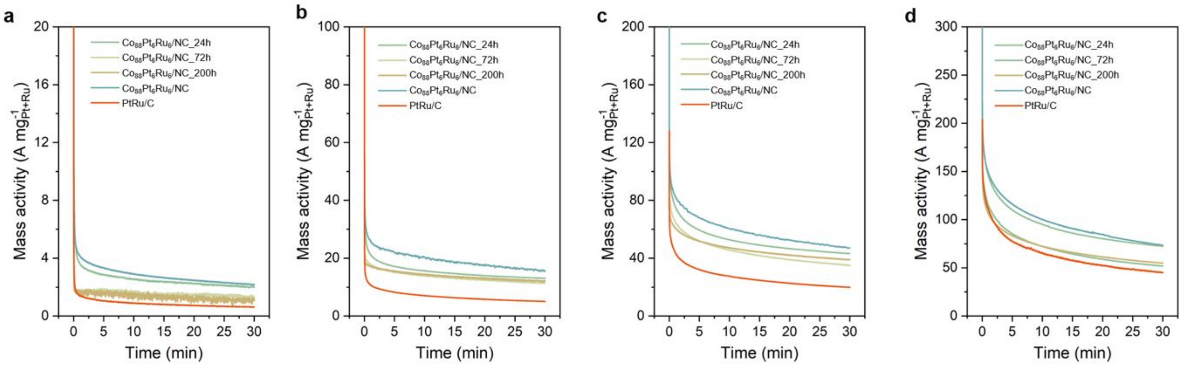

Figure S37. Mass activity of CA measurements for $Co_{88}Pt_6Ru_6$/NC after acid treatment and compared with $Co_{88}Pt_6Ru_6$/NC before acid treatment and commercial PtRu/C. The applied potential is 0.4 V (a), 0.5 V (b), 0.6 V (c), and 0.7 V (d) vs. RHE.

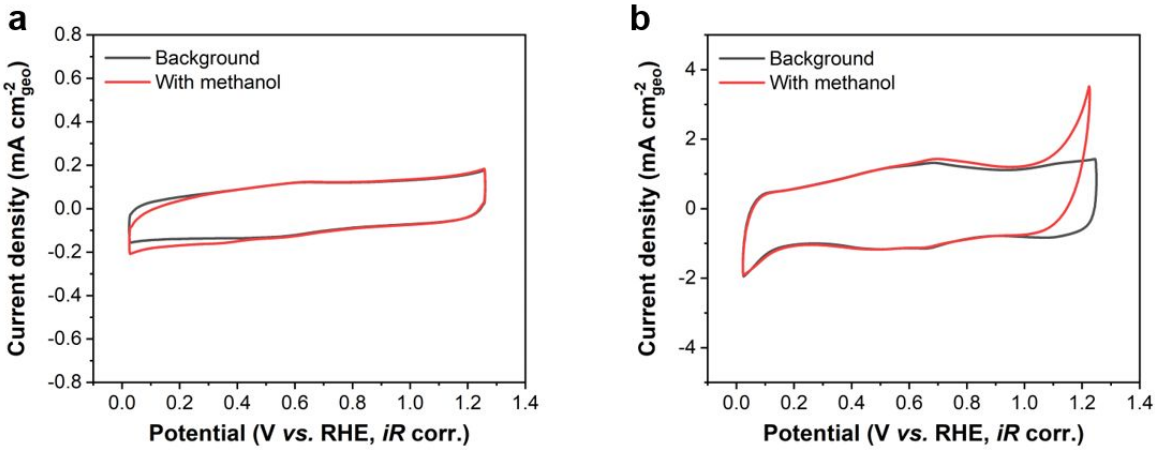

Figure S38. MOR measurements for Co NPs/NC (a) and Co-Ru/NC (b).

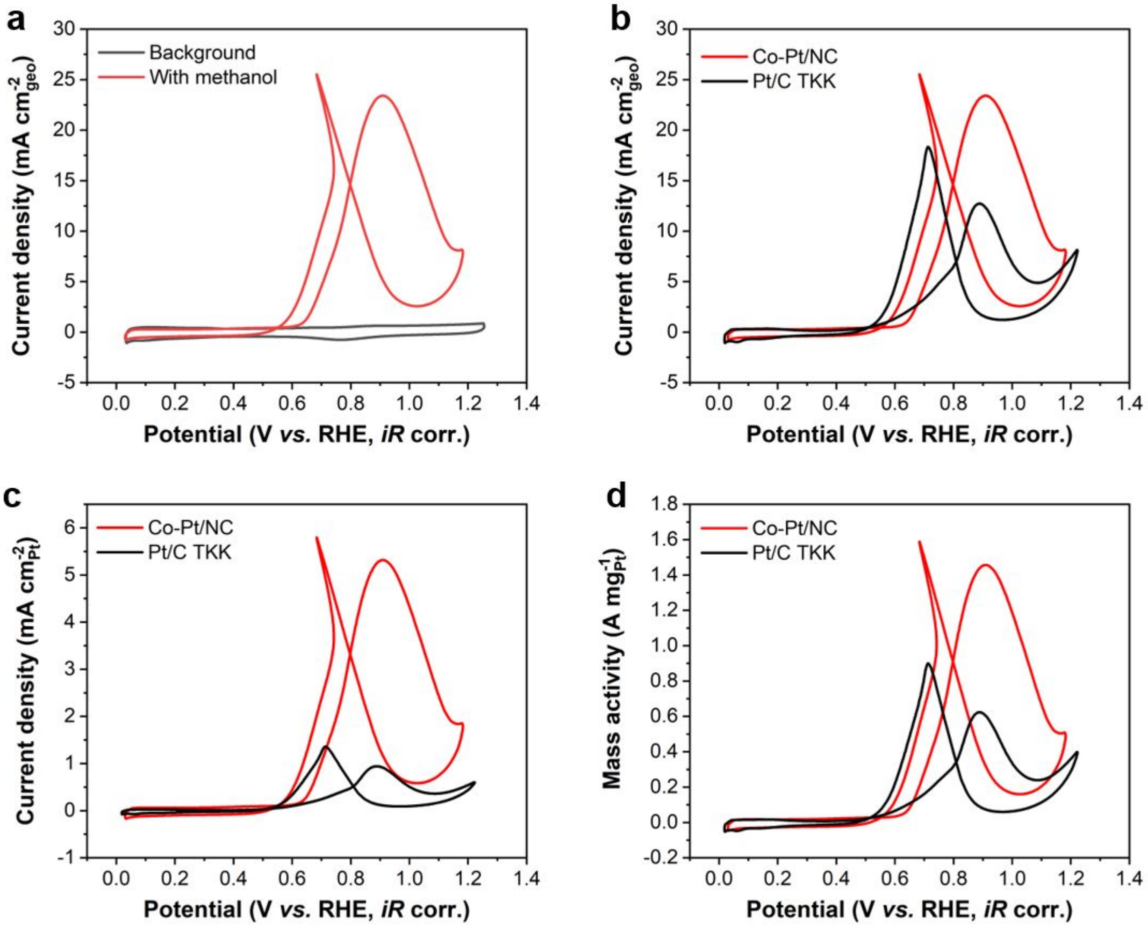

Figure S39. MOR CV results of Co-Pt/NC and compared with commercial Pt/C catalyst. (a) Background and with methanol for Co-Pt/NC. (b) Geometrical activity. (c) Specific activity. (d) Mass activity. The CV was measured in Ar-saturated 0.1 M $HClO_4$ solution with 1 M CH_3OH at a scan rate of 50 mV s^{-1}.

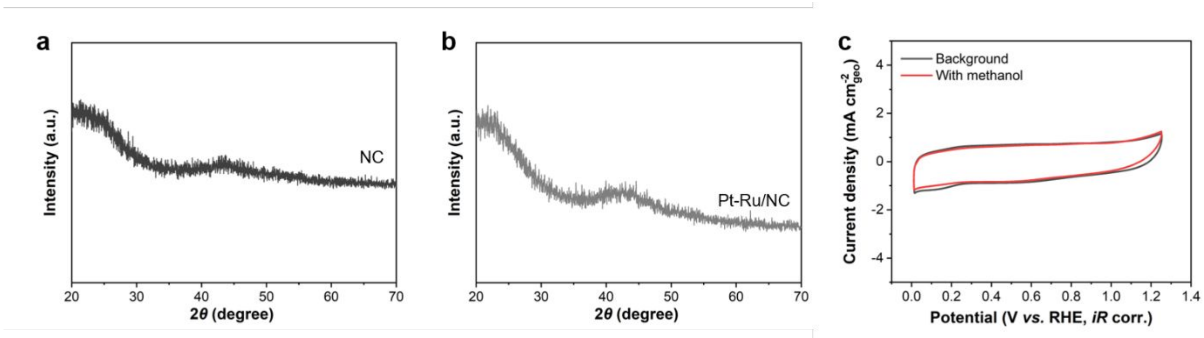

Figure S40. (a) XRD pattern of ZIF-8 after pyrolysis. (b) XRD pattern of Pt-Ru/NC. (c) MOR measurements for Pt-Ru/NC.

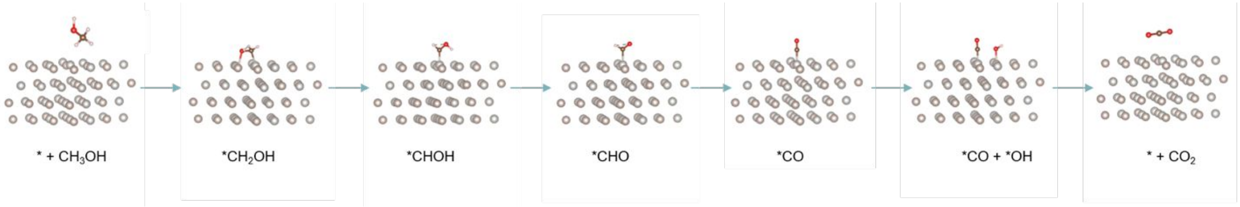

Figure S41. Reaction pathway for MOR on PtRu/C.

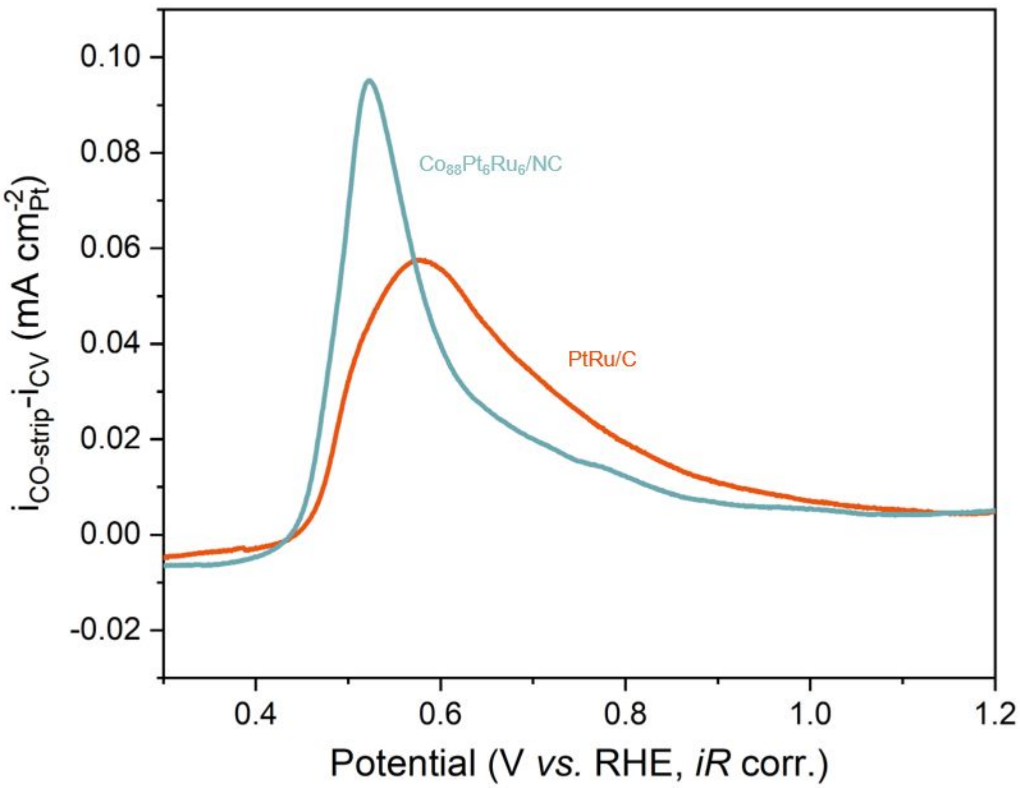

Figure S42. The CO stripping current (background-corrected) measured via potential sweep at 10 mV/s in 0.1 M $HClO_4$ on PtRu/C and $Co_{88}Pt_6Ru_6$/NC catalysts.

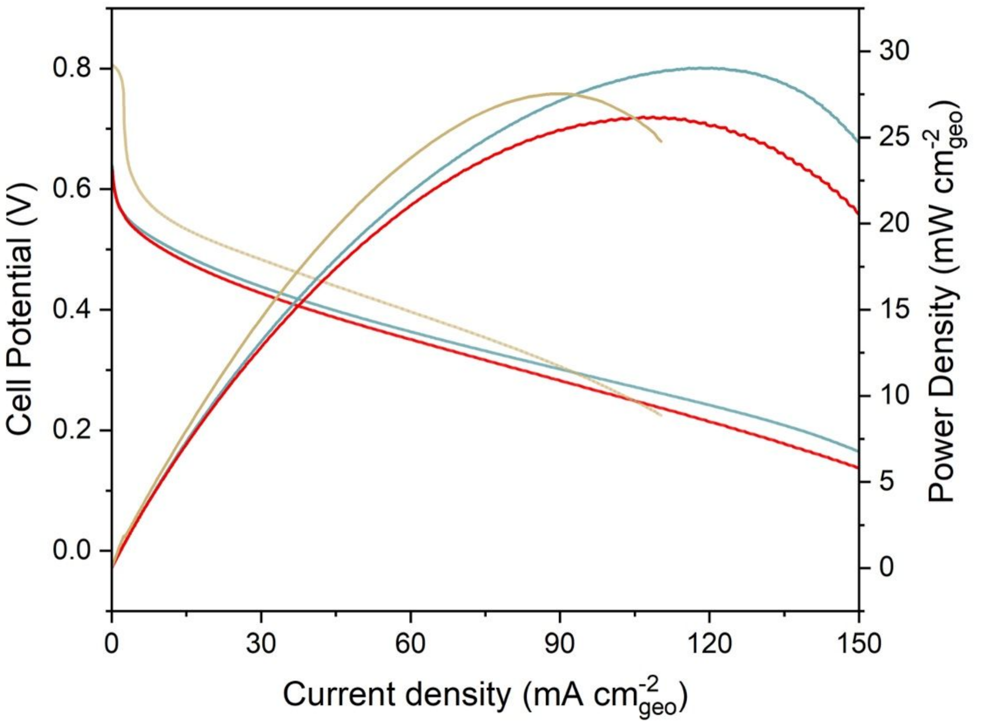

Figure S43. Repeat experiments of DMFCs performance of $Co_{88}Pt_6Ru_6/NC$ catalysts at the anode with 1 M methanol at 60°C.

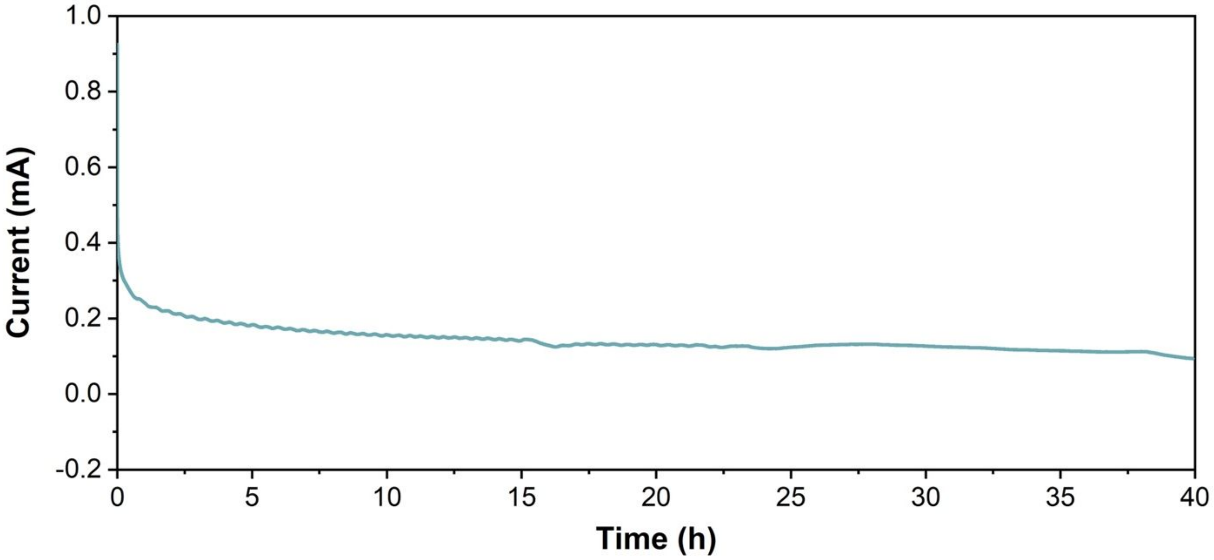

Figure S44. Stability test of $Co_{88}Pt_6Ru_6$/NC catalyst for MOR by CA method in three-electrode system. The current decreased ~70 % at first 10 hours and was stable after further 30 hours.

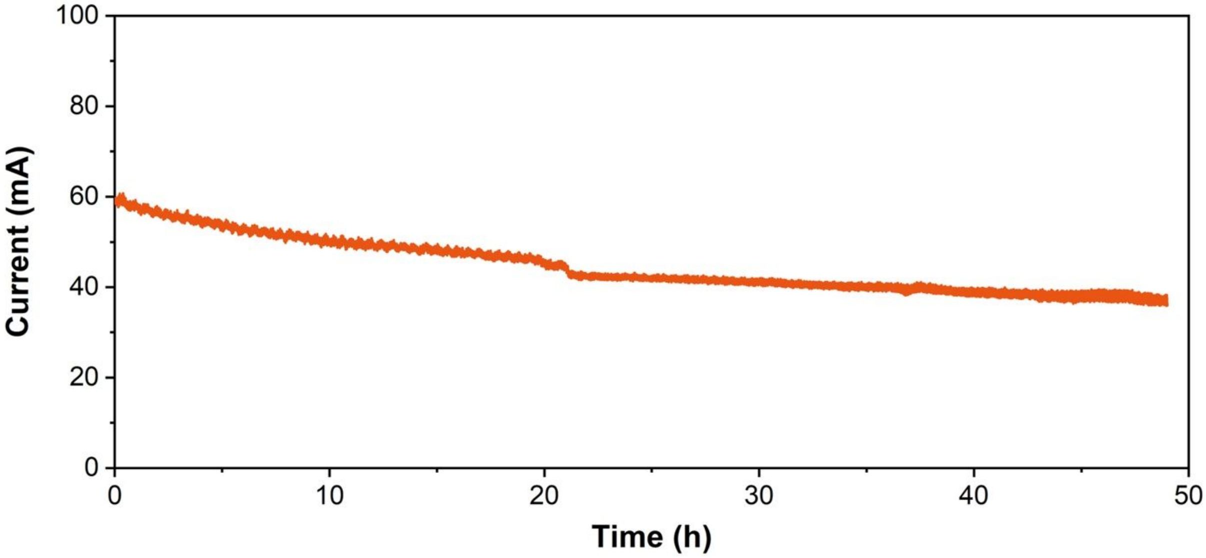

Figure S45. Stability test of $Co_{88}Pt_6Ru_6/NC$ catalyst for DMFC by CA method for 48 hours.

Table S1. The comparison of MOR activity to the state-of-the-art Pt and PtRu-based catalysts at 0.6 V vs RHE. The results of our work are *iR*-corrected and background-corrected.

Materials	Electrolyte	Geometric activity (mA cm^{-2})	Specific activity (mA cm$^{-2}_{Pt}$)	Mass activity (A mg$^{-1}_{Pt+Ru}$)	Ref
$Co_{\mathbf{88}}Pt_{\mathbf{6}}Ru_{\mathbf{6}}$/NC	0.1 M $HClO_4$ + 1.0 M CH_3OH	7.61±2.38	2.14±0.24	0.28±0.06	Our work
Commercial PtRu/C	0.1 M $HClO_4$ + 1.0 M CH_3OH	1.48	0.48	0.072	Our work
$Co_{88}Pt_6Ru_6$/NC_24h	0.1 M $HClO_4$ + 1.0 M CH_3OH	3.37	1.13	0.15	Our work
$Co_{88}Pt_6Ru_6$/NC_72h	0.1 M $HClO_4$ + 1.0 M CH_3OH	3.77	1.36	0.15	Our work
$Co_{88}Pt_6Ru_6$/NC_200h	0.1 M $HClO_4$ + 1.0 M CH_3OH	4.16	1.21	0.14	Our work
Single Pt atoms on Ru	0.1 M $HClO_4$ + 1.0 M CH_3OH	10	0.52	0.091	3
Pt island on Ru	0.1 M $HClO_4$ + 1.0 M CH_3OH	3.0	0.24	0.039	3
Commercial PtRu	0.1 M $HClO_4$ + 1.0 M CH_3OH	1.8	0.38	0.072	3
$Au_{0.5}Pt_{0.5}$	0.1 M $HClO_4$ + 1.0 M CH_3OH	-	0.18±0.01	0.027 (Metal)	4
$Pt_{72}Ru_{28}$	0.1 M $HClO_4$ + 0.5 M CH_3OH	-	2.1	0.25	5
PtNiRh NWs/C	0.1 M $HClO_4$ + 0.5 M CH_3OH	-	0.33	0.23 (Pt)	6
PtRu nanodenderites	0.1 M $HClO_4$ + 0.5 M CH_3OH	0.3	0.72	0.078 (Pt)	7
PtRuCu hexapods/C	0.1 M $HClO_4$ + 1.0 M CH_3OH	-	0.14	0.035 (Pt)	8
Pt/Ru-RuO_2	0.5 M H_2SO_4 + 2.0 M CH_3OH	-	-	0.06 (Pt)	9
h-PtNiCo/C	0.1 M $HClO_4$ + 0.5 M CH_3OH	-	0.20	0.1 (Pt)	10

Ru-ca-PtNi	0.1 M $HClO_4$ + 0.5 M CH_3OH	1.0	0.18	0.075 (Pt)	11
$PtRu_{c-s}$	0.1 M $HClO_4$ + 1.0 M CH_3OH	-	1.1	-	12

Note: The bracket after mass activity represents the metals used to normalize.

Table S2. The comparison of MEA performance.

Materials	Methanol concentration (M)	Test temperature (°C)	PtRu loading (mg cm^{-2})	Geometric activity (mW cm^{-2})	Mass activity (mW mg^{-1}_{Pt+Ru})	Ref
$Co_{88}Pt_6Ru_6$/NC	1	60	0.6	27.6±1.4	46±2.3	Our work
Commercial PtRu/C	1	60	2	23.6	11.8	Our work
PtRu/C + 20%IrO_2	2	60	2	23	11.5	13
PtRu/C (house-made)20%	1	70	2.5	44	17.6	14
PtRu/C(E-TEK)20%	1	70	2.5	42	16.8	14
PtRu(1:1)/ MWCNT	2	70	15.2	32	2.1	15
PtRu/MWCNTs	2	70	2.1	54.6	26	16
PtRu/f-MWNT	1	60	2.5	21	8.4	17
PtRu/(50 wt% f-MWNT D 50 wt% f-G)	1	60	2.5	29	11.6	17
PtRu	2	70	5	160	32	18
PtRuRhNi	2	70	5	180	36	18
PtRu black	1	60	4	72.3	18.1	19
Carbon-supported PtRu	8	60	2	78	39	20

Table S3. Contributions to the adsorbate free energy from the zero-point energy correction, enthalpic temperature correction, entropy, and the total free energy correction, respectively. All values are given in eV[21].

Adsorbates	G_corr
Slab	0
CO	0.115
CO_OH	0.446
COOH	0.542
CHO	0.346
CHOH	0.492
CH_2O	0.659
CH_2OH	1.022

References

1. Peterson, A. A., Abild-Pedersen, F., Studt, F., Rossmeisl, J. & Nørskov, J. K. How copper catalyzes the electroreduction of carbon dioxide into hydrocarbon fuels. *Energy Environ Sci* **3**, 1311-1315 (2010).
2. Nørskov, J. K. et al. Origin of the overpotential for oxygen reduction at a fuel-cell cathode. *J. Phys. Chem. B* **108**, 17886-17892 (2004).
3. Poerwoprajitno, A. R. *et al.* A single-Pt-atom-on-Ru-nanoparticle electrocatalyst for CO-resilient methanol oxidation. *Nat Catal* **5**, 231–237 (2022).
4. Suntivich, J. *et al.* Surface Composition Tuning of Au–Pt Bimetallic Nanoparticles for Enhanced Carbon Monoxide and Methanol Electro-oxidation. *J. Am. Chem. Soc.* **135**, 7985–7991 (2013).
5. Zhao, W.-Y. *et al.* Highly Active and Durable $Pt_{72}Ru_{28}$ Porous Nanoalloy Assembled with Sub-4.0 nm Particles for Methanol Oxidation. *Adv. Energy Mater.* **7**, 1601593 (2017).
6. Zhang, W. *et al.* Ultrathin PtNiM (M = Rh, Os, and Ir) Nanowires as Efficient Fuel Oxidation Electrocatalytic Materials. *Adv. Mater.* **31**, 1805833 (2019).
7. Lu, S. *et al.* One-pot synthesis of PtRu nanodendrites as efficient catalysts for methanol oxidation reaction. *Nanoscale* **9**, 1033–1039 (2017).
8. Xue, S. *et al.* Hexapod PtRuCu Nanocrystalline Alloy for Highly Efficient and Stable Methanol Oxidation. *ACS Catal.* **8**, 7578–7584 (2018).
9. An, G.-H., Lee, E.-H. & Ahn, H.-J. Ruthenium and ruthenium oxide nanofiber supports for enhanced activity of platinum electrocatalysts in the methanol oxidation reaction. *Phys. Chem. Chem. Phys.* **18**, 14859–14866 (2016).
10. Ma, H. *et al.* Trimetallic PtNiCo branched nanocages as efficient and durable bifunctional electrocatalysts towards oxygen reduction and methanol oxidation reactions. *J. Mater. Chem. A* **9**, 23444–23450 (2021).
11. Kong, F. *et al.* Selectively Coupling Ru Single Atoms to PtNi Concavities for High-Performance Methanol Oxidation via *d* -Band Center Regulation. *Angew Chem Int Ed* **61**, (2022).
12. Hunt, S. *et al.* Self-assembly of noble metal monolayers on transition metal carbide nanoparticle catalysts. *Science* **352**, 974-978 (2016).

13. Baglio, V. *et al.* Composite anode electrode based on iridium oxide promoter for direct methanol fuel cells. *Electrochimica Acta* **128**, 304–310 (2014).
14. Guo, J. W., Zhao, T. S., Prabhuram, J., Chen, R. & Wong, C. W. Preparation and characterization of a PtRu/C nanocatalyst for direct methanol fuel cells. *Electrochimica Acta* **51**, 754–763 (2005).
15. Prabhuram, J., Zhao, T. S., Tang, Z. K., Chen, R. & Liang, Z. X. Multiwalled Carbon Nanotube Supported PtRu for the Anode of Direct Methanol Fuel Cells. *J. Phys. Chem. B* **110**, 5245–5252 (2006).
16. Prabhuram, J., Zhao, T. S., Liang, Z. X. & Chen, R. A simple method for the synthesis of PtRu nanoparticles on the multi-walled carbon nanotube for the anode of a DMFC. *Electrochimica Acta* **52**, 2649–2656 (2007).
17. Jha, N., Jafri, R. I., Rajalakshmi, N. & Ramaprabhu, S. Graphene-multi walled carbon nanotube hybrid electrocatalyst support material for direct methanol fuel cell. *International Journal of Hydrogen Energy* **36**, 7284–7290 (2011).
18. Park, K. W. *et al.* PtRuRhNi nanoparticle electrocatalyst for methanol electrooxidation in direct methanol fuel cell, *Journal of Catalysis*, **224**, 236-242, (2004)
19. Wang, Z. B. *et al*. Catalyst failure analysis of a direct methanol fuel cell membrane electrode assembly, *Journal of Power Sources*, **177**, 386-392, (2008)
20. Kang, K., Lee, G., Gwak, G., Choi, Y. & Ju, H. Development of an advanced MEA to use high-concentration methanol fuel in a direct methanol fuel cell system, *International Journal of Hydrogen Energy* **37**, 6285-6291 (2012).
21. Peterson, A. A., Abild-Pedersen. F, Studt, F., Rossmeisl, J., Norskov, J., How copper catalyzes the electroreduction of carbon dioxide into hydrocarbon fuels. *Energy Environ. Sci.***,** **3**, 1311-1315 (2010).